

Investigation of the biophysical basis for cell organelle morphology

Diplomarbeit
zur Erlangung des wissenschaftlichen Grades
Diplom - Physiker

vorgelegt von
Jürgen Mayer
geboren am 14.03.1977
in Biberach

Max-Planck-Institut für Molekulare Zellbiologie und Genetik
Fachrichtung Physik
Fakultät für Mathematik und Naturwissenschaften
Technische Universität Dresden
2008

1. Gutachter: Prof. Jonathon Howard
2. Gutachter: Prof. Petra Schwille

Datum des Einreichens der Arbeit: 12. Februar 2008

Abstract

It is known that fission yeast *Schizosaccharomyces pombe* maintains its nuclear envelope during mitosis and it undergoes an interesting shape change during cell division - from a spherical via an ellipsoidal and a peanut-like to a dumb-bell shape. However, the biomechanical system behind this amazing transformation is still not understood. What we know is, that the shape must change due to forces acting on the membrane surrounding the nucleus and the microtubule based mitotic spindle is thought to play a key role. To estimate the locations and directions of the forces, the shape of the nucleus was recorded by confocal light microscopy. But such data is often inhomogeneously labeled with gaps in the boundary, making classical segmentation impractical. In order to accurately determine the shape we developed a global parametric shape description method, based on a Fourier coordinate expansion. The method implicitly assumes a closed and smooth surface. We will calculate the geometrical properties of the 2-dimensional shape and extend it to 3-dimensional properties, assuming rotational symmetry. Using a mechanical model for the lipid bilayer and the so called Helfrich-Canham free energy we want to calculate the minimum energy shape while respecting system-specific constraints to the surface and the enclosed volume. Comparing it with the observed shape leads to the forces. This provides the needed research tools to study forces based on images.

Zusammenfassung

Es ist wohlbekannt, dass die Spaltheife *Schizosaccharomyces pombe* während der Mitose ihren Zellkern aufrechterhält, welcher dafür einen interessanten Gestaltwandel durchläuft - von einem anfänglich sphärischen über einen ellipsoiden und erdnussähnlichen bis hin zu einem hantelförmigen Gebilde. Der zugrundeliegende biomechanische Mechanismus, der hinter dieser faszinierenden Verwandlung steckt, ist bis heute unbekannt. Es müssen Kräfte auf die Zellkernmembran wirken und man geht davon aus, dass die aus Mikrotubuli bestehende polare Spindelfaser hierbei eine entscheidende Rolle spielt. Um Ort und Richtung der wirkenden Kräfte zu bestimmen, wird der Zellkern mittels konfokaler Lichtmikroskopie erfasst. Die hierbei oft ungleichmässige Markierung kann zu Lücken in der Umrandung führen, wodurch klassische Segmentierungstechniken nur schwer nutzbar sind. Um dennoch die Gestalt genau zu bestimmen entwickelten wir eine parametrische Beschreibungsmethode, die auf Fourierreihenentwicklung basiert. Diese Methode geht implizit von einer geschlossenen, glatten Oberfläche aus. Es werden sowohl die geometrischen Eigenschaften der zweidimensionalen Kontur berechnet, als auch diejenigen, die bei der Rotation dieser Kontur entstehenden Dreidimensionalen. Mit Hilfe des Lipid-Doppelschichten-Modells, bei dem keine Scherfestigkeit angenommen wird, wollen wir die minimalenergetische Gestalt unter Vorgabe von Randbedingungen wie der Oberfläche und dem eingeschlossenen Volumen berechnen. Die Kräfte können dann aus dem Vergleich mit der tatsächlich vorkommenden Form gewonnen werden. Damit können wir Kräfte untersuchen, die auf Bildinformationen beruhen.

Contents

1	Introduction	1
1.1	General Introduction	1
1.2	Biological background	2
1.2.1	The nucleus	3
1.2.2	Labeling with Cut11-GFP	5
1.3	Confocal fluorescence microscopy	8
1.3.1	Principles of laser scanning confocal microscopy	8
1.3.2	The Point-Spread-Function	8
1.3.3	Microscope setup	10
1.3.4	Sample preparation	11
2	Methods	13
2.1	Fourier series and Fourier expansion	13
2.1.1	Introduction to Fourier series	13
2.1.2	Fourier series representation	16
2.1.3	Fourier coordinate expansion	17
2.1.4	Meaning of the coefficients	21
2.2	The 2-d-contour-explorer	23
2.3	Shape analysis	25
2.3.1	Decreasing amplitudes and truncation of the series	25
2.3.2	Calculating the 2-dimensional properties	26
2.3.3	Program testing	30
2.3.4	The Elephant	31
2.4	Application to confocal images	33
2.4.1	From the coefficients to the shape	33
2.4.2	From the shape to the coefficients	34
2.4.3	Bending energy and the L-curve	38
2.5	Extension to 3-d	40
2.5.1	Calculating the 3-dimensional properties	42
2.5.2	Program testing	44
2.5.3	Alignment	45
3	Conclusions and Outlook	49
A	Protocol	51
B	List of abbreviations	53

List of Figures

1.1	Confocal images, <i>S. pombe</i> strain PG2747	3
1.2	Electron microscopic image of a <i>S. pombe</i> cell during prophase .	4
1.3	Excitation- and emission spectrum of GFP	6
1.4	Sequence of a Cut11-GFP labeled nucleus, cell strain: FN41 . . .	7
1.5	Principal beamline in a confocal microscope	9
2.1	Gibbs phenomenon	15
2.2	The sine cardinal (sinc) function	15
2.3	Lanczos σ factors	15
2.4	Cartesian and polar representation	17
2.5	Symmetric shapes	19
2.6	Constraints for symmetry	20
2.7	Best fit ellipse	23
2.8	The 2-d-contour-explorer interface	24
2.9	The letter E: 1 st order approximation	26
2.10	The letter E: 4 th and 10 th order approximation and their spectra	27
2.11	The letter E: 35 th order approximation and its spectrum	28
2.12	Three rotating phasors	29
2.13	The elephant: original image, frequency spectrum and the wig- gling trunk	32
2.14	Discrete representation and uniform intensity profile of an ellipse	34
2.15	χ^2 and corresponding amplitudes	37
2.16	The L-curve	39
2.17	Comparison of data and resulting contour for different λ values .	40
2.18	3-d reconstruction of the nucleus during telophase	42
2.19	Calculated Gaussian and mean curvature compared with the an- alytic results	46

List of Tables

2.1	Basic shapes and their coefficients	18
2.2	Test results for the circle	31
2.3	Test results for the ellipse	31
2.4	5 parameters encoding the elephant including its wiggling trunk .	33
2.5	Comparison of calculated properties and analytic results for the sphere	45
2.6	Comparison of calculated properties and analytic results for a prolate and an oblate spheroid	47

1

Introduction

1.1 General Introduction

Forces are important for life, not only on a macroscopic but also on a microscopic scale. They organize things (and therein reduce the entropy) by directed movement, for example in cells. *Schizosaccharomyces pombe* is a frequently used model organism and a well investigated biological system. Understanding its cell cycle helps in cancer research and contributes knowledge about the phenomenon of aging. In this project we focus on the nucleus and examine its morphogenesis. There are descriptions of interphase nuclear geometry [47] using simulated annealing, but there are no models to describe the complex morphological changes of mitotic nuclei. The shape transformations are thought to be driven by the intranuclear mitotic spindle, but the mechanical basis is still not known. First we highlight the biological background in section 1.2 and explain the used terms. As we record confocal images, a short overview about confocal microscopy and the used setup is given in section 1.3. We assume the observed system to be quasi-static during the time of imaging one particular stage. The method to analyze the acquired images is based on Fourier series. A similar approach has been used for confocal images of red blood cells [43], but using spherical harmonics. In section 2.1 the concepts and the advantages of using this technique are presented. The determination of a set of parameters (only few) that globally encodes a given shape provides a powerful tool for shape description. Using continuous basis functions, we get rid of any resolution limitations imposed by the mesh (section 2.3). The key step of connecting the confocal image with a set of parameters, that can be used to calculate geometrical properties and the difficulties in determining them is illustrated in section 2.4. All the programs used therefor (besides 2 image-batch-processing ones, that are adapted from Saleh and Tolić-Nørrelykke, both working at MPI-CBG, Dresden, Germany) were developed and written by myself using MATLAB®. To deduce the forces acting on the nucleus we have to calculate the minimum energy shape by fixing the boundary conditions of surface area and volume (invoking Lagrange multipliers) and minimizing an energy functional. In this model the area difference elasticity [20] is not considered. The energy is calculated using the mean squared curvature integrated over the entire surface. The prediction is that there is a phase transition between shapes that can be described by the used model and

shapes of later stages, that require additional constraints like the overall length along the long axis (that can be provided by the mitotic spindle).

1.2 Biological background

The fission yeast *Schizosaccharomyces pombe* (*S. pombe*) is a unicellular eukaryote belonging to the Ascomycetes (fungi). It is a rod-shaped cell that grows by elongation at its ends. Division occurs by the formation of a septum, or cell plate, in the center of the rod [4]. *S. pombe* has been found to be one of the best experimental models for the study of cell cycle control [29] and its mechanisms of cell cycle control are remarkably similar to mammalian ones. This makes it a rewarding subject for investigation in cancer research. The eukaryotic cell cycle is divided into four major phases [50]. During the synthesis (S) phase the DNA is replicated, followed by a gap phase (G_2) to prepare and check all conditions that have to be met for proper continuation. The next step is the mitotic (M) phase, consisting of mitosis and cytokinesis. Mitosis in turn is subdivided into several stages: During the prophase, the chromosomes condense by tightly folding loops. The chromosomes become aligned at the equator, ready for segregation during metaphase. In anaphase, the sister chromatids separate and move to the opposite poles of the spindle (in case of yeast cells). As a last mitotic step, the decondensation of the separated chromosomes takes place in telophase and the physical division of the cytoplasm (cytokinesis) results in two daughter cells. They enter another gap phase (G_1), that is - apart from cell growth - especially important to monitor the internal and external environment and to assure all preparations are being completed. The cycle is closed by entering again in S phase now. G_1 , S and G_2 together are called interphase. In rapidly dividing *S. pombe* cells, the S phase follows so shortly the nuclear division, that nearly all the newly separated daughter cells emerge as G_2 cells from the start [22].

Generally in eukaryotic cells, microtubules (MTs) [39] play an important role in cell dynamics and cell polarity. During interphase in *S. pombe*, they position the nucleus at the center of the yeast cell, forming a basket of 6 - 8 MTs. They are anti-parallel spanned along the long axis of the cell, with their plus end pointing towards the cell tips and the minus end overlapping in the vicinity of the nucleus [55]. All of them are entirely cytoplasmic. MTs generally start to polymerize from microtubule-organizing centers (MTOCs). In fission yeast a specialized MTOC, called the spindle pole body (SPB) [17], is the origin of nucleating spindle MTs, that occur within the nucleus at the beginning of mitosis. In late G_2 phase the SPB has duplicated and the two SPBs are moved to opposite sides of the nucleus. At this time the interphase MTs in the cytoplasm depolymerize. Concerning the spindle in *S. pombe*, mitosis can be described in three steps: i) spindle formation (prophase) and subsequently spindle elongation to span the nucleus in prometaphase. ii) period of constant spindle length (metaphase plus anaphase A), where alignment of the chromosomes between the poles and separation of the sister chromatids occur. iii) spindle elongation (anaphase B), where the two poles pull the two genomes to either end of the cell [69], [22]. The focus of this project lies on the nucleus during anaphase B, telophase and cytokinesis. So the nucleus is regarded in more detail.

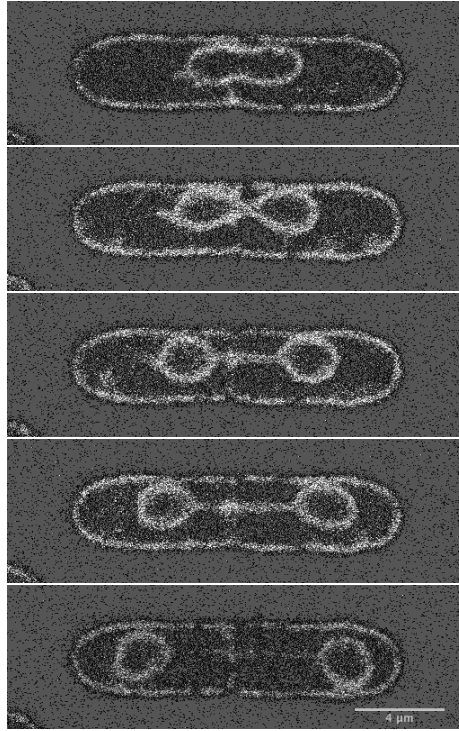


Figure 1.1: Confocal images of a *S. pombe* strain PG2747, genotype: h^{90} , *leu1-32 ura4-D18 ade6-216* [D817] during division (telophase to cytokinesis). The inner structure (ellipsoid, peanut, dumbbell) is the nucleus, the surrounding structure belongs to the yeast cell membrane. Time interval between subsequent pictures is 120 seconds, scale bar is 4 μm . Pictures are kindly provided by Tolić-Nørrelykke-group, MPI-CBG, Dresden, Germany. Note that the dumbbell-shaped nucleus is explicitly derived in Figure 2.5(d).

1.2.1 The nucleus

In common with other fungi, the nuclear envelope (NE) remains intact throughout mitosis. It consists of a bilayer of lipids [3], which are amphiphilic molecules [9]. More precise, it is a system of two lipid bilayers that are thought to be connected at the nuclear pores (for details about the nuclear pore complex see next section). There is found no lamina that provides structural support to the NE, so that we have a pure lipid bilayer (neglecting membrane proteins) and therein no extra shear resistance. Even if there is a lamina analog in fission yeast, it does not influence the NE geometry during interphase [47]. The mechanical properties of fission yeast nuclei and vesicles consisting of lipid bilayers are therein very similar. Also during interphase the nuclear size doubles, corresponding to the doubling of the chromosomes during each cell cycle. Whereas all the volume increase occurs completely during interphase, the surface increases partly in interphase, partly in M phase [47]. So there must be a different area to volume ratio during mitosis, explaining the nonspherical shapes of the nucleus to some extent. In order to increase the surface area, the NE must be connected to an external membrane reservoir (for mitosis most likely the endoplasmatic

reticulum), because lipid bilayers lacking this reservoir can only sustain a small area increase ($\leq 5\%$) without disruption [61]. The SPB is considered a key role for proper division and an indispensable part for anchoring the intranuclear MTs [54] like the spindle to the membrane. An improper anchored spindle or absence of one of the SPBs (via the *msd1* null mutant [71], or *mia1* overexpression [77]) on elongating nuclear spindles leads to formation of a tether at the side of the mis-anchored or missing SPB, whereas the opposite well-anchored or SPB-containing side remains undeformed [47]. The SPB is permanently associated with the NE. During interphase it consists of a main body on the outside of the NE, but always has a raft of material on the nucleoplasmic side directly beneath and connected to the main body [17]. Entering mitosis, the SPB becomes embedded in the NE membrane. This insertion of the mitotic SPB into the NE requires cut11p (see next section). The most important in-

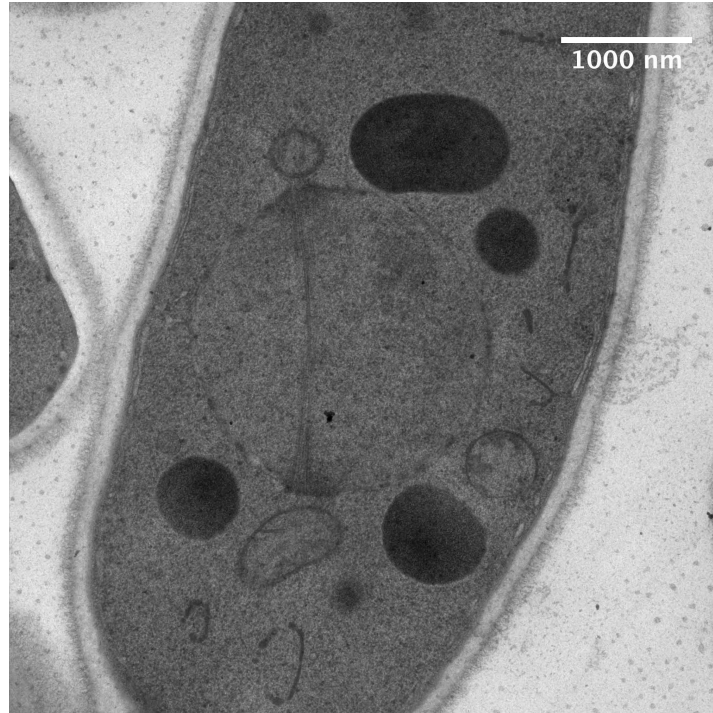


Figure 1.2: Electron microscopic image of a *S. pombe* cell during prophase. The big circular shape within the cell is the nuclear membrane. The dimmer parts on the nuclear membrane are the spindle pole bodies and they are connected via the bipolar spindle, which consists of microtubules. The mitotic spindle moves the spindle pole bodies to opposing sites of the nucleus such that the spindle gets aligned to the long axis of the cell. The smaller, dark filled structures are vacuoles and the small ring-like contours mitochondria. Scale bar is 1 μm . The image is kindly provided by M. Storch, MPI-CBG, Dresden, Germany.

tranuclear MTs for our considerations are those, that are thought to push the two poles away from each other. They grow from one SPB towards the other (polar MTs) and interdigitate at the midzone, where kinesin-like proteins (Klp) crosslink the spindle MTs [65], [69]. The Klp moves towards the polymerizing

MT plus ends (away from the nucleation site of the MT at the SPB) and as they connect MTs of opposite direction, they push away the SPBs from each other. The interdigitating MTs from the two SPBs interact in a way that forms a mechanically stable bundle [16] and therefore increases the flexural rigidity [30]. This bundle can clearly be seen in Figure 1.2 (in an early stage, where the SPBs still move towards opposing sides and get aligned along the long-axis of the cell). The SPBs also link intranuclear spindle MTs with cytoplasmic astral MTs, that start to grow tangentially to the NE into the cytoplasm at anaphase (for details see [34]). One might imagine some cytoplasmic MTs like the astral MTs anchored at opposite cell ends pulling the spindle poles apart, but it is highly unlikely in *S. pombe* since a substantial astral pull was not found and the pulling motor (dynein) is not essential for proper mitosis [69].

1.2.2 Labeling with Cut11-GFP

Fluorescence is some kind of luminescence process in which susceptible molecules are electronically excited. By relaxation back to their ground state they emit light. The energy level system is typically illustrated by a Jablonski diagram [57]. When a photon is being absorbed whose energy matches the distance between the ground state and some non-ground state of that fluorophore, it will be excited into a vibrational state within the excited singlet band. The rate of excitation per fluorophore is proportional to the excitation intensity $I[W/cm^2]$ and is calculated by $\alpha_{ex} = \frac{I\sigma}{h\nu}$, where $\sigma[cm^2]$ is the wavelength-dependent absorption cross section and $h\nu$ the absorbed photon energy [56].

The fluorophore relaxes radiationless and very quickly ($\sim 10^{-12}s$) to the lowest vibrational state within the singlet band, leading to the so-called Stokes shift [33] and therefore to the difference in the excitation and emission spectra (see Figure 1.3). The desired fluorescence emission that can occur by falling back to its ground state has to compete with other processes like intersystem crossing (where a spin-flip occurs that leads to an energetically lower, intermediate state with a much longer lifetime \rightarrow phosphorescence) and photobleaching (where the dye molecule changes chemically to a non-fluorescent one).

As photobleaching, Rayleigh and Raman scattering [44] as well as autofluorescence depend on the intensity I , they are limiting factors for increasing α_{ex} by only raising the intensity. The scattering and the autofluorescence further increase the background signal and decrease contrast therein, because they don't saturate as fast as the desired fluorescence signal does [57]. GFP [48] (Green fluorescent protein) is such a fluorophore described above. The excitation and emission spectra of GFP can be seen in Figure 1.3 (see Legend for details). It is a relatively small (≈ 27 kDa) protein and very convenient for labeling biological samples, especially if the sample is not fixed and intracellular delivery to the structure of interest (SOI) is complicated. Unlike quantum dots that almost always require invasive methods, GFP can be synthesized and folded *in situ*. Thus, the most elegant way to label the desired region inside a cell is, to express GFP together with a protein that localizes at this specific region. Here the NE is the SOI, making the nuclear pore complex (NPC) a promising candidate. The NPC forms the exclusive conduit to exchange macromolecules between the nucleus and the cytoplasm, making it an important control point for the regulation of gene expression. In yeast it is a large structure with a molecular weight of ≈ 66 MDa. Around 200 of the NPC are distributed over the nucleus [2] and

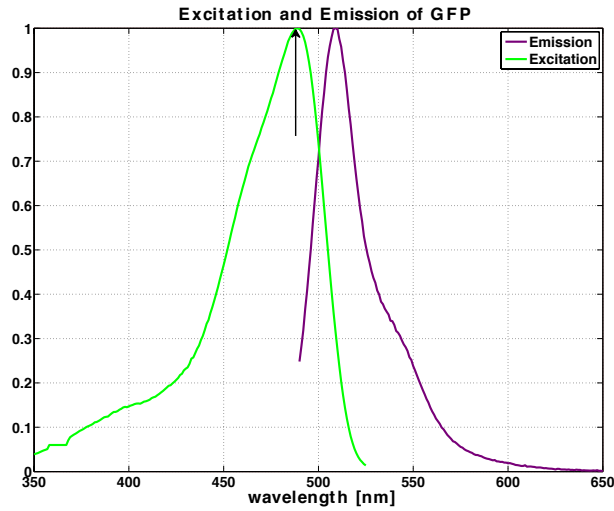


Figure 1.3: The excitation- and emission spectrum of GFP. The green line displays the receptivity of the fluorophore according to the wavelength of the exciting light, the so called absorption bands. The red one shows the composition of the emitted light. The black arrow indicates the wavelength of the exciting laser. The plot is based on data provided by George McNamara on the PubSpectra website, available under <http://home.earthlink.net/~pubspectra>

they are embedded in the pore membrane domain of the NE, where the inner and outer nuclear membranes fuse [64].

Cut11-GFP, which localizes constitutively to the NPC as well as to the mitotic and meiotic SPBs [70] hence stains precisely the NE for fluorescence microscopy in a non-invasive manner. Cut11p itself is thought to anchor the NPC (and additionally the SPBs from prophase to early anaphase) in the NE [75] and therefore is an integral-like protein (it sits in the membrane instead of just being attached to it). The accumulation of cut11p around the embedded SPBs leads to cumulative staining and subsequently to the bright spots seen in Figure 1.4 in the first few stages. Not using Cut11-GFP would consequently suppress the bright spots of labeled SPBs. A possible disadvantage of using the NPC-related Cut11-GFP for labeling the membrane could be, that there are potentially no such NPC in the axial tube that connects the two bulbs of the dumbbell-shape in later stages of the nuclear division. At least this could explain the bad signal of the tube compared to other methods of staining the membrane like S. Baumgärtner (Tolić-Nørrelykke group, MPI-CBG, Germany) used for the images in Figure 1.1. Baumgärtner took the *S. pombe* strain PG2747, genotype: *h90, leu1-32 ura4-D18 ade6-216* [D817]. The plasmid D817 harbours NADPH-cytochrome (SPBC365.17) P450 reductase-GFP under its natural promotor (see [1] and [52] for details). This means NADPH-cytochrome P450 reductase-GFP (with a molecular weight of 76 kDa + 27 kDa from GFP) is the membrane-labeling protein. It is integral to the membrane alike the NPC, but much smaller. It labels the membrane material less specifically, so the outer membrane is also visible.

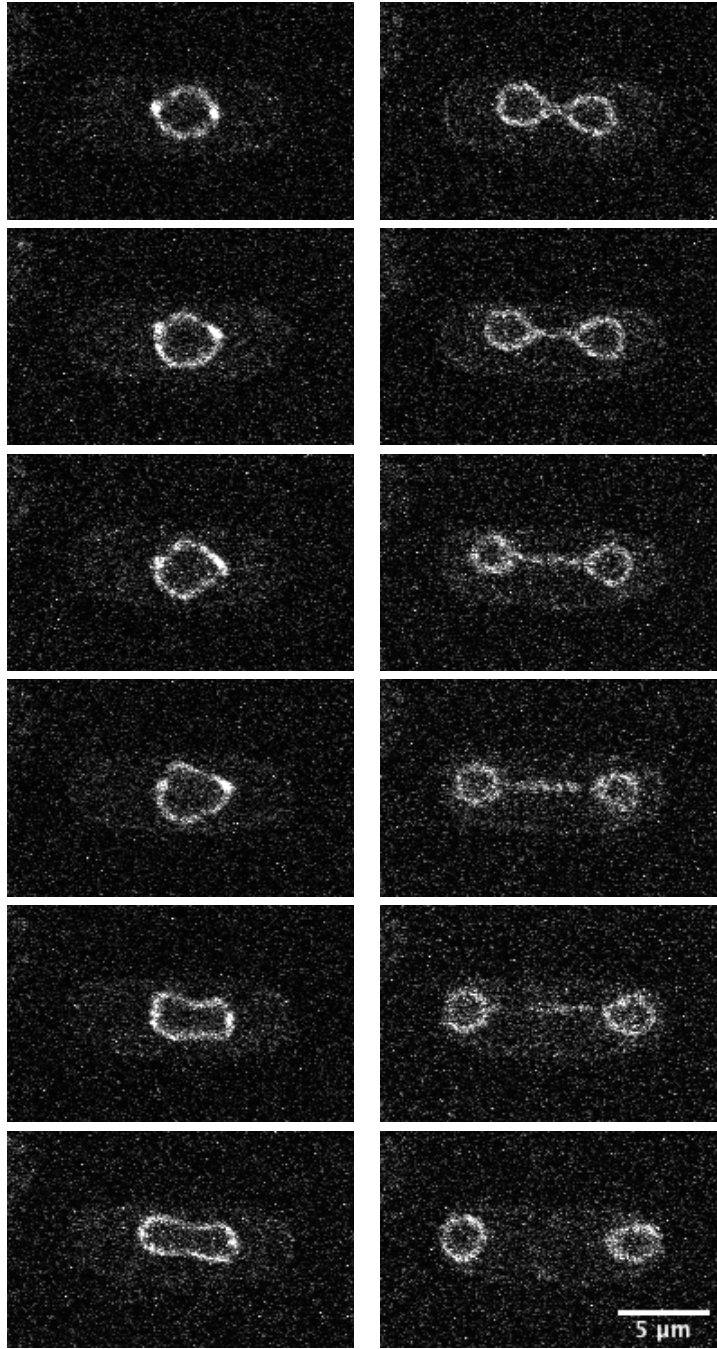


Figure 1.4: Sequence of a Cut11-GFP labeled nucleus (cell strain: FN41 *cut11-GFP-ura4 + ura4-D18, h⁻*) from telophase to cytokinesis. These pictures are used for analyzation (Also compare the dumbbell shapes to Figure 2.5(d)). The bright spots in the membrane of pictures in the left row are the spindle pole bodies. The region slightly brighter than the background defines the cell outline. Time step between subsequent pictures (top to bottom, left to right) is 120 s. Scale bar is 5 μm .

1.3 Confocal fluorescence microscopy

This technique of imaging is based on fluorescent dyes (like Cut11-GFP described in section 1.2.2) being excited by a focal spot of laser light. The excitation wavelength (here: $\lambda_{ex} = 488$ nm) is being separated from the emission wavelength (here: $\lambda_{em} = 510$ nm) by a dichroic mirror (here: 405/488), which serves basically as a wavelength-dependent beam-splitter. The specification 405/488 means that light with a wavelength of 405 ± 5 nm and 488 ± 5 nm will be blocked and hence that it deflects excitation light and transmits the red-shifted fluorescence, which in turn can be detected without the outshine of the exiting light (see Figure 1.3 and 1.5).

1.3.1 Principles of laser scanning confocal microscopy

A laser scanning confocal microscope (LSCM) is not much different from a conventional scanning microscope but it allows a better control of the depth by suppressing the out-of-focus information as well as an enhanced lateral resolution. The first one because of the fact that only information of a thin region in the neighborhood of the focal plane is detected. This is done by the pinhole which is situated in a plane conjugate to the intermediate image plane and thus in the focus of the lens. All light from outside the focal plane will be blocked by the pinhole as one can see following the dashed vertical line in Figure 1.5. The spatial separation gives rise to optical sectioning [76] and therein the 3-dimensional reconstruction of the imaged structure by connecting the slices. The latter one - the lateral resolution - is dependent on the contrast, which in turn is dependent on the signal-to-noise ratio. Any contrast reduction decreases the cut-off distance and therefore degrades the resolution. A better signal-to-noise ratio therein increases also lateral resolution. The pinhole blocks scattered light so that it helps to suppress noise. The coordinate system is defined here as follows: x and y representing the lateral dimension and so the orientation of the focal plane (see Figure 1.5). They also refer to the axes of the detector plane. The z -axis is perpendicular to the focal plane and therefore displays the depth of the object.

One of the big advantages of confocal microscopy is the non-destructive visualization that allows recording the evolution of one and the same cell over time. Visualizing membrane structure and organelle morphology by electron microscopy has improved [5] and would give a higher resolution (see images in Figure 1.2), but requires fixation and preparation of the sample.

1.3.2 The Point-Spread-Function

Any object imaged by an optical microscope will be blurred by processes like diffraction, scattering, refractive index mismatches (e.g. between immersion oil and sample) and general imperfections in optical components. The mathematical function to describe this process is called the point spread function (PSF). It is simply the pattern that one single point (it must be smaller as the used wavelength) provokes in the image plane after having passed through the optical system. The object is convoluted with the PSF to give the image

$$I(x, y, z, t) = O(x, y, z, t) \otimes \text{PSF}(x, y, z, t) \quad (1.1)$$

beampath in a confocal microscope

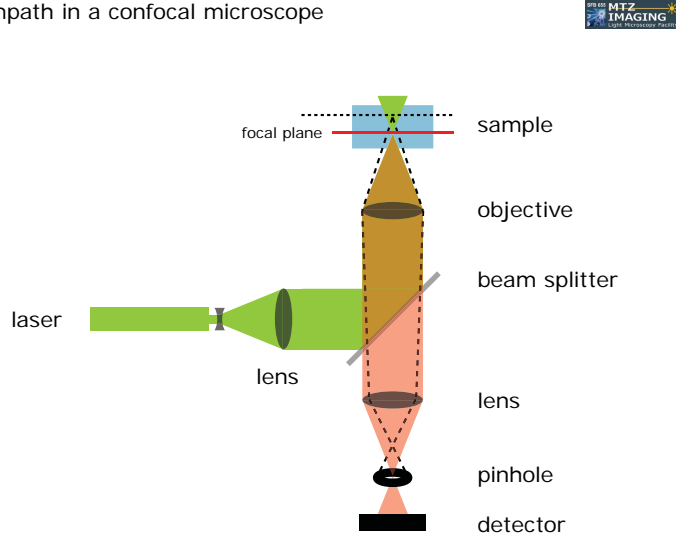


Figure 1.5: Principal beamline: The exciting laser light (green) is deflected by the beam splitter and focused at the sample in the focal plane. The dye is excited and emits light of longer wavelength (red) than the exciting one. The emitted light is transmitted by the beam splitter and detected after passing the pinhole. Note that the specimen has to be moved for scanning the sample in the focal plane. Another possibility would be to invoke a deflection mirror that enables the focus to be moved. Drawing from MTZ Light Microscopy Facility, Dresden, Germany.

where I is the image and O the object. The symbol \otimes denotes convolution of O and PSF . If we take the Fourier transform \mathcal{F} of equation (1.1), the \otimes becomes an ordinary multiplication

$$\mathcal{F}[I(x, y, z, t)] = \mathcal{F}[O(x, y, z, t)] \cdot \mathcal{F}[PSF(x, y, z, t)] \quad (1.2)$$

This is an important feature for image deconvolution. The full-width-half-maximum (FWHM) of the PSF in lateral ($W_{x,y}$) and axial direction (W_z) can be approximated by [56]

$$W_x = W_y = \frac{0.47 \cdot \lambda}{\eta \sin(\alpha)} \quad \text{and} \quad W_z = \frac{0.44 \cdot \lambda}{\eta \sin^2(\alpha/2)} \quad (1.3)$$

where λ is the wavelength of the used light (here: $\lambda_{em} = 510$ nm), η the refractive index of the medium between the specimen and the objective (here: immersion oil $\eta = 1.518$) and $\alpha = \sin^{-1}(NA/\eta)$ the semi-aperture angle of the objective. (NA denotes the numerical aperture.) With these values specified we get

$$W_x = W_y \approx 177 \text{ nm} \quad \text{and} \quad W_z \approx 544 \text{ nm}$$

The lateral extension is the same in x - and y -direction as the PSF is rotationally symmetric about the z -axis. In z -direction, the main intensity is distributed ellipsoidal with the semi-major axis aligned (prolate).

1.3.3 Microscope setup

Olympus Fluoview

The microscope used in this work is an Olympus FV-1000. It is an inverted laser scanning confocal microscope. An oil immersion objective (ULSAPO 60x) with NA = 1.35 was used. The immersion oil refractive index is $\eta = 1.518$. An argon laser with a wavelength of 488 nm was chosen to excite the fluorophore. In this setup the diameter of the pinhole is 105 μm . Together with the objective magnification (60x), the system magnification (3.82 - provided by Olympus engineers) the backprojected pinhole radius is calculated to ≈ 229 nm. Backprojected means the size of the pinhole as it appears in the specimen plane: the physical pinhole size r_{phys} divided by the total magnification of the detection system. This total magnification is the product of the (usually variable) objective magnification times a fixed internal magnification: $r_{backfocal} = \frac{r_{phys}}{m_{obj} \cdot m_{sys}}$ where m_{obj} is the magnification factor of the objective and m_{sys} is the fixed magnification of the system (see also: <http://support.svi.nl/wiki/NyquistCalculator>). This calculated backprojected pinhole radius matches with the optical resolution (Rayleigh criterion) of about 200 nm to get best possible results. The Rayleigh criterion shortly displays the necessary separation of two self-luminous point sources such that their diffraction patterns show a detectable drop in intensity between them.

The detector is a photomultiplier tube (PMT) sensitive to light of 494 - 545 nm. Binning of registered photons into a raster of pixels makes it reasonable to divide the optical resolution by at least a factor of about 2 to avoid the loss of information. This is explained by the Nyquist sampling rate that roughly says: If you want to convert an analog signal into a digitized one, you have to use a sampling rate of at least two times the highest frequency of the actual analog signal. The chosen pixel resolution of 98 nm/pixel in both directions (x and y) satisfies the criterion. Any much finer sized raster would not improve the amount of information and a coarser one would produce undersampling, reducing the recorded brightness of small features. As the image size here is 120 by 192 pixels it represents 11.7 by 18.8 μm .

Z -resolution (the distance between subsequent z -stacks) is 300 nm. As 14 different z -slices are taken, the overall scanning depth is 3.9 μm , slicing the whole nucleus (the average size of a *S. pombe* nucleus is 7-15 μm in length and around 4 μm in diameter [29]). One could blame for oversampling as the PSF in z -direction was calculated to 544 nm (using equation 1.3) and subsequently there is always a part of information from neighboring z -stacks in the actual slice. But oversampling is not critical and only increases the amount of data - assuming that it is not an exaggerated oversampling, because this would imply either more damage to the dye by longer excitation or fewer photons/pixel - explained by the sampling speed.

Sampling speed in turn is a critical value and always a compromise between signal quality and bleaching. Usually, the longer the dwell time on a particular pixel, the more signal will be detected and the less it will be distorted by Poisson noise. On the other side the longer the laser focus excites a certain region, the more bleaching will occur and the worse the signal will become over time. The used 12.5 μs /pixel is such a compromise. Time intervals between subsequent series of z -stacks are chosen to be $\Delta t = 2$ min. This is a good balance

between the recording of all the different shapes of the nucleus and minimization of photodamage for not losing so much signal quality over time. $590 \mu\text{W}$ is the optimal laser power calculated to balance between fluorophore excitation and background-increasing events (autofluorescence, Raman and Rayleigh scattering) [57].

Zeiss UV

Most of the features are similar to the Olympus setup, that only the main settings are mentioned.

- Objective: Plan Apochromat 63x/1.4 oil DIC
- Excitation wavelength 488 nm
- Longpass filter 505
- Pinhole radius: $104 \mu\text{m}$
- Pixel time 5-6 μs
- x, y -resolution: mostly 80 nm
- z -resolution: 300 nm

1.3.4 Sample preparation

The used *S. pombe* strain (FN41 *cut11-GFP-ura4 + ura4-D18, h⁻*) was cultured and bountiful provided by I. Raabe (Tolić-Nørrelykke group, MPI-CBG, Germany). The EMM (Edinburgh Minimal Medium; for details see Appendix on page 53) is used to nourish the culture both in the case of solid and liquid culturing.

First, 4-5 ml of liquid EMM is inoculated by taking a swab of a solid cultured strain. This so called preculture is incubated at 25°C for 24 hours. Then, ≈ 1 ml of the preculture is used to inoculate 50 ml of a fresh EMM, that is subsequently incubated for another 24 hours. This culture now is used to prepare the sample. Lectin (2 mg/ml) is given on a coverslip (No. 1.5) and dried. This serves as a glue to fix the yeast cells. Silikon at the rim of the coverslip is used to attach it to the previously prepared Microwell dish (35 mm petri dish, 10 mm microwell) in a way, that the glutinous part of the coverslip is freely accessible through the hole in the bottom of the dish. The silicon seals the gap between coverslip and dish, so that the final culture can be dripped onto without leaking. After sedimentation for about 10 minutes, the not yet settled cells are carefully washed away. The dish is filled with fresh EMM during all the time of imaging.

2

Methods

2.1 Fourier series and Fourier expansion

An arbitrary complicated shape is not trivial to describe without using a large number of parameters or losing generality. Polygon or chain code approximations would require a lot of segments to describe a general contour. To overcome this problem, we use the Fourier expansion up to frequencies where the amplitudes are negligible. We developed a tool (that we will call *2d-contour-explorer*) to create significantly different shapes by manipulating very few parameters. Obvious not completely closed contours as they may occur in confocal images due to a partially bad fluorescence signal or imperfect labeling will be automatically represented as closed structures, making it an interesting kind of description for life sciences. Even if there are only a few dots along the contour, the mathematical description by Fourier series (FS) contains all the intermediate points due to the use of continuous basis functions (see next section).

2.1.1 Introduction to Fourier series

Every regular (without singularities), periodic function $f(x)$ can be represented by a infinite sum of sines and cosines (the basis functions).

$$f(x) = \frac{a_0}{2} + \sum_{n=1}^{\infty} [a_n \cos(n \cdot x) + b_n \sin(n \cdot x)] \quad (2.1)$$

where the coefficients calculate to

$$a_n = \frac{1}{\pi} \int_{-\pi}^{\pi} f(x) \cos(n \cdot x) dx \quad b_n = \frac{1}{\pi} \int_{-\pi}^{\pi} f(x) \sin(n \cdot x) dx \quad \text{and} \quad a_0 = \frac{1}{\pi} \int_{-\pi}^{\pi} f(x) dx$$

These are the so called Fourier coefficients. The only limitations that have to be set on $f(x)$ are:

1. $f(x)$ has only a finite number of maxima and minima
2. $f(x)$ has only a finite number of (finite) discontinuities
3. $f(x)$ must be 2π -periodic

For even functions $b_n = 0$ and the series reduces to

$$f_{\text{even}}(x) = \frac{a_0}{2} + \sum_{n=1}^{\infty} a_n \cos(n \cdot x)$$

likewise for odd functions, where $a_n = 0$, it becomes

$$f_{\text{odd}}(x) = \sum_{n=1}^{\infty} b_n \sin(n \cdot x)$$

The derivatives are easily calculated, as one can see e.g. for the first derivative

$$f'(x) = \frac{df(x)}{dx} = 0 + \sum_{n=1}^{\infty} [n\{b_n \cos(n \cdot x) - a_n \sin(n \cdot x)\}] \quad (2.2)$$

The Fourier coefficients are the amplitudes of the diverse frequencies (the so called harmonics [41]). They weight every frequency to define how much this particular frequency contributes to the whole function. Usually the low frequencies are more important, as they already give a crude approximation. The higher the frequencies, the more details they represent.

Note, that the sum goes up to infinity. However, in most cases it is sufficient to respect the first N terms and to neglect all frequencies greater than a certain N . There is an interesting tool available at <http://www.falstad.com/fourier/> to visualize how the number of harmonics affect the accuracy of representing a given function. It can also be seen in Figure 2.1, which shows a different number of low order harmonics trying to fit the given (rectangular) function. The FS in this special case becomes

$$f(x) = \frac{4}{\pi} \sum_{n=1,3,5,\dots}^N \frac{1}{n} \sin(n \cdot x) \quad (2.3)$$

The peculiarity that additionally can be seen in this figure is the behavior near a (finite) discontinuity, called Gibbs phenomenon. This leads to certain difficulties when such a finite series is used to compute a value of this function near its discontinuity. It is clear that the first N terms of a FS cannot fit the infinite slope demanded by the discontinuity. The overshooting at the upper end of the discontinuity is equal to the undershooting at the lower end. The over- and undershooting together is calculated to be $\approx 18\%$ of the 'jump' [66]. However, this can be removed by the Lanczos sigma factor [74]. The FS then becomes

$$f(x) = \frac{a_0}{2} + \sum_{n=1}^{m-1} \text{sinc}\left(\frac{n\pi}{m}\right) [a_n \cos(n \cdot x) + b_n \sin(n \cdot x)] \quad (2.4)$$

where m is the last term and $\text{sinc}(\frac{n\pi}{m})$ are the Lanczos σ factors. The sinc function's full name is 'sine cardinal' and is defined as

$$\text{sinc}(x) = \begin{cases} 1 & x = 0 \\ \frac{\sin(\pi x)}{\pi x} & \text{otherwise} \end{cases} \quad (2.5)$$

It is displayed in Figure 2.2. The function of the above definition is the contin-

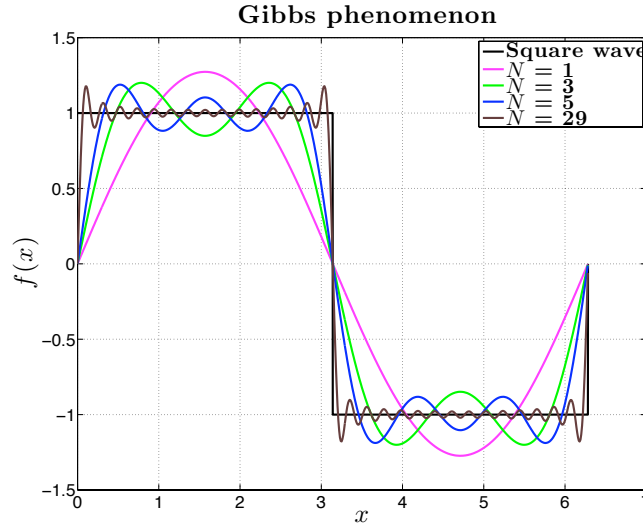


Figure 2.1: As explained in the text, there is a natural over- and undershooting at the discontinuities (the Gibbs phenomenon), even if high frequencies are included in the Fourier series (FS). All the functions are plotted from 0 to 2π . The black line is the given rectangular function. The colored graphs show the different adaption level by using equation (2.3) with different values for N . In red, only the first harmonic is considered and thus it shows the ordinary sine function. The more harmonics are included, the better the FS fits to the original function.

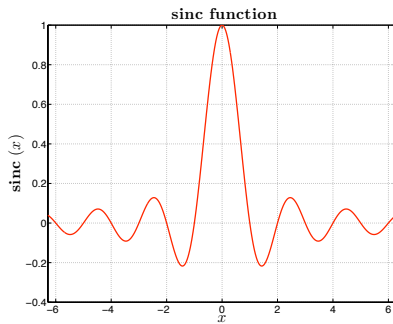


Figure 2.2: The sine cardinal (sinc) function as defined in equation (2.5) displayed from -2π to 2π . If it would be defined like $\text{sinc}(x) = \frac{\sin(x)}{x}$ for $x \neq 0$ (and $\text{sinc}(x) = 1$ for $x = 0$), it would turn out that $\text{sinc}(x) \equiv j_0(x)$ (spherical Bessel function of the first kind).

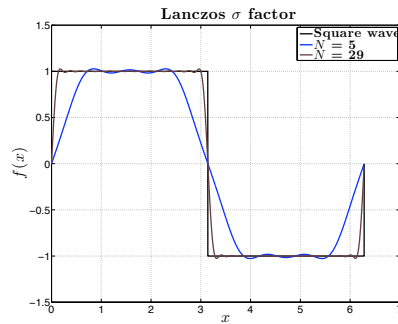


Figure 2.3: Removing of over- and undershooting by Lanczos σ factors (equation (2.4) is used). Comparing the graphs in this Figure with the corresponding ones in Figure 2.1 shows the much better adaption to the given function. (The rectangular function (black) is the same in both figures.)

uous inverse Fourier transform of a rectangular pulse of width 2π and height 1. There are alternative definitions (see [74]), but in any case it is closely related to the spherical Bessel function of the first kind $j_0(x)$. A different but equivalent description [8] of the FS is

$$f(x) = \frac{a_0}{2} + \sum_{n=1}^{\infty} A_n \sin(n \cdot x + \varphi_n) \quad (2.6)$$

where in this case $A_n = \sqrt{a_n^2 + b_n^2}$ and $\tan \varphi_n = \frac{a_n}{b_n}$. If we represent the series in its extended complex form (by replacing $\cos(n \cdot x) = \frac{1}{2}(e^{inx} + e^{-inx})$ and $\sin(n \cdot x) = \frac{1}{2i}(e^{inx} - e^{-inx})$ in equation (2.1) it becomes

$$f(x) = c_0 + \sum_{n=1}^{\infty} (c_n e^{inx} + c_{-n} e^{-inx}) = \sum_{n=-\infty}^{\infty} c_n e^{inx} \quad (2.7)$$

where i is the complex number and $c_n = \frac{1}{2\pi} \int_{-\pi}^{\pi} f(x) e^{-inx} dx$, $n = 0, \pm 1, \pm 2, \dots$. Note that the coefficients can be written as

$$c_n = \begin{cases} \frac{1}{2\pi} \int_{-\pi}^{\pi} f(x) [\cos(n \cdot x) + i \sin(n \cdot x)] dx & = \frac{1}{2}(a_{-n} + ib_{-n}) & \text{for } n < 0 \\ \frac{1}{2\pi} \int_{-\pi}^{\pi} f(x) dx & = \frac{1}{2}a_0 & \text{for } n = 0 \\ \frac{1}{2\pi} \int_{-\pi}^{\pi} f(x) [\cos(n \cdot x) - i \sin(n \cdot x)] dx & = \frac{1}{2}(a_n - ib_n) & \text{for } n > 0 \end{cases}$$

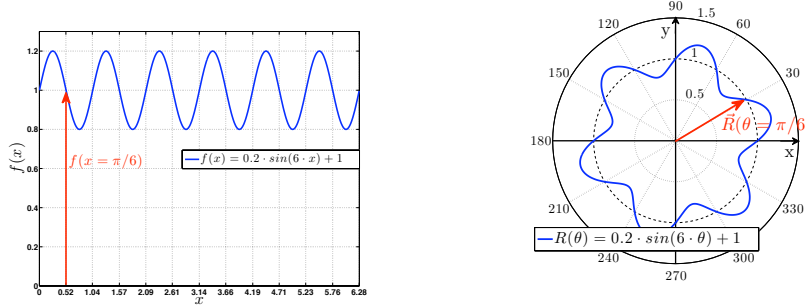
Moreover the c_n are the basis for the Fourier transform, which is obtained by denoting $c_n = \frac{1}{L} \int_{-L/2}^{L/2} f(x) e^{-i(\frac{2\pi n}{L}x)} dx$ and converting the discrete c_n to a continuous $F(k)$ by letting the length of the periodic function $L \rightarrow \infty$, while letting $\frac{n}{L} \rightarrow k$.

2.1.2 Fourier series representation

All the properties of the previous section are maintained when we map the function to another representation like a polar one. The function is then 'wrapped' on a circle and $x \mapsto \theta$ while $f(x) \mapsto R(\theta)$. In Figure 2.4(b) can be seen that θ denotes the angle between the x-axis and the radius-vector \vec{R} , where θ ranges from 0 to 2π . Now the radius of a contour is expressed as a FS by

$$R(\theta) = \sum_{k=0}^{\infty} (a_k \cos(k \cdot \theta) + b_k \sin(k \cdot \theta)) \quad (2.8)$$

As all sine- and cosine-terms in the infinite sum are at least 2π -periodic the contour is closed. The $\pi/3$ -periodicity of the function plotted in Figure 2.4 leads to a 6-fold symmetry in the polar representation. (More about symmetry in section 2.1.3). An amazingly high number of completely different shapes can be produced by varying the amplitudes of the first 10 harmonics only, whereas the rest of the coefficients is being kept to zero. Note that all sequences $\{c_n\}$ for which the series in equation (2.7) converges describe closed curves [59]. However, one big disadvantage still remains: As $R(\theta)$ is a unique function, we are limited to star-like shapes !



(a) Usual cartesian representation

(b) Mapped polar representation

Figure 2.4: In both figures the same function is plotted. In figure (a) it is represented in cartesian coordinates, whereas in figure(b) it is mapped to polar coordinates. The function value f becomes the length of the \vec{R} -vector and the x -coordinate the angle between the x -axis and the \vec{R} -vector. The angle is denoted counterclockwise. The graph in figure (b) is closed, due to the 2π -periodicity of the function. The additional $\pi/3$ -periodicity causes the observed 6-fold symmetry. A cartesian coordinate system is superimposed to the polar coordinate system.

2.1.3 Fourier coordinate expansion

To create non-star-like shapes we expand x and y separately in a complete Fourier expansion and then represent every point of the contour with a pair (x, y) . Both x and y depend on a parameter t that is to be considered different from the angle θ as defined for equation (2.8). One can think of a parametric 2-dimensional vector \vec{p} , where x and y are the components

$$\vec{p}(t) = \begin{pmatrix} x(t) \\ y(t) \end{pmatrix} \quad (2.9)$$

The parameter t then can be seen as the arc length (see 'Concept of a Curve' [49]), or more advanced: The time when we trace out the way along the curve (yet at constant velocity). Assuming that we prevent self-intersection, every pair $(x(t), y(t))$ determines a unique point on the perimeter for every different t . The two expansions that we have to consider now are

$$x(t) = \sum_{k=0}^{\infty} (A_k^x \cos(k \cdot t) + B_k^x \sin(k \cdot t)) \quad (2.10)$$

$$y(t) = \sum_{k=0}^{\infty} (A_k^y \cos(k \cdot t) + B_k^y \sin(k \cdot t)) \quad (2.11)$$

with the A_k^x , B_k^x , A_k^y and B_k^y being the coefficients. The upper indices are not to be mistaken for exponents ! In the following we will always refer to this parametric expansion of equations (2.10) and (2.11) and their coefficients.

All coefficients $k \geq 2$ can be normalized by the 'radius of the 1st harmonic circle' ($\sqrt{[A_1^x]^2 + [B_1^x]^2}$ respectively for x and y) to get relative amplitudes, but we just keep in mind, that we use absolute values.

Székely et al. [68] used the same approach for the parameterization of 2-D contours in their segmentation of midsagittal MR (magnetic resonance) images. They used it as a basis for Fourier snakes, whereas we will use a different method (see section 2.4). Kuhl and Giardina [45] in turn used the Fourier series expansion successfully in combination with chain-encoded contours. They therefore used well defined contours where subsequent pixels are 8-connected, so that it is unstated how the procedure will deal with noise. (In 2-D, pixels are 8-connected if their edges or corners touch and so subsequent pixels are connected along the horizontal, vertical or diagonal direction.) A different approach worked out by Gielis [28] is the 'Superformula' which is based on a tuned ellipsoidal equation. It is also a powerful tool regarding the creation of diverse shapes by changing few parameters, but without intersection it cannot create closed non-starlike contours.

Simple shapes

To show the simplicity of obtaining very basic shapes like a circle or an ellipse, see some examples in Table 2.1. Already here it becomes clear that there is

	A_1^x	B_1^x	A_1^y	B_1^y
Circle	1	0	0	1
Ellipse oblate	1	0	0	< 1
Ellipse prolate	< 1	0	0	1

Table 2.1: The most basic shapes and their coefficients. All higher harmonics ($k \geq 2$) are equal to zero. This is just one example, there are other possible combinations to create the very same shapes. Changing the values of $A_1^x \leftrightarrow B_1^x$ **and** $A_1^y \leftrightarrow B_1^y$ for example will not change the resulting shapes (but the orientation of the tangent vector \rightarrow see chapter 2.3.2). Also an arbitrary chosen $k \neq 1$ is valid, when all other harmonics except the chosen one are set to zero. In this case the same shape will be drawn k times.

not only one set of coefficients unambiguously connected to a particular shape. In the regarded case of high symmetric shapes (circle and ellipse) exists even an infinite number of possible sets that describe the identical shapes ! Fixing the values of the amplitudes in Table 2.1 makes it clear. The subindex k can be chosen arbitrarily without changing the resulting shape. Like in the case $k = 1$ (which is displayed in the table), where all other amplitudes $k \neq 1$ must have been equal to zero, we just have to set all amplitudes to zero that are not corresponding to the k^{th} harmonic that has been chosen. The circle or ellipse will then be drawn k times.

A few remarkable things can be seen in the slightly less basic shapes displayed in Figure 2.5. First, cusps and spicules may arise already at low harmonics, resulting in highly curved regions. Second, almost straight lines can be produced that are connected by sharp edges. Note that only harmonics $k \leq 5$ are used. Third, there is the 'proof' that non-starlike shapes are easily obtained. Remarks about the symmetry will be made in the next section.

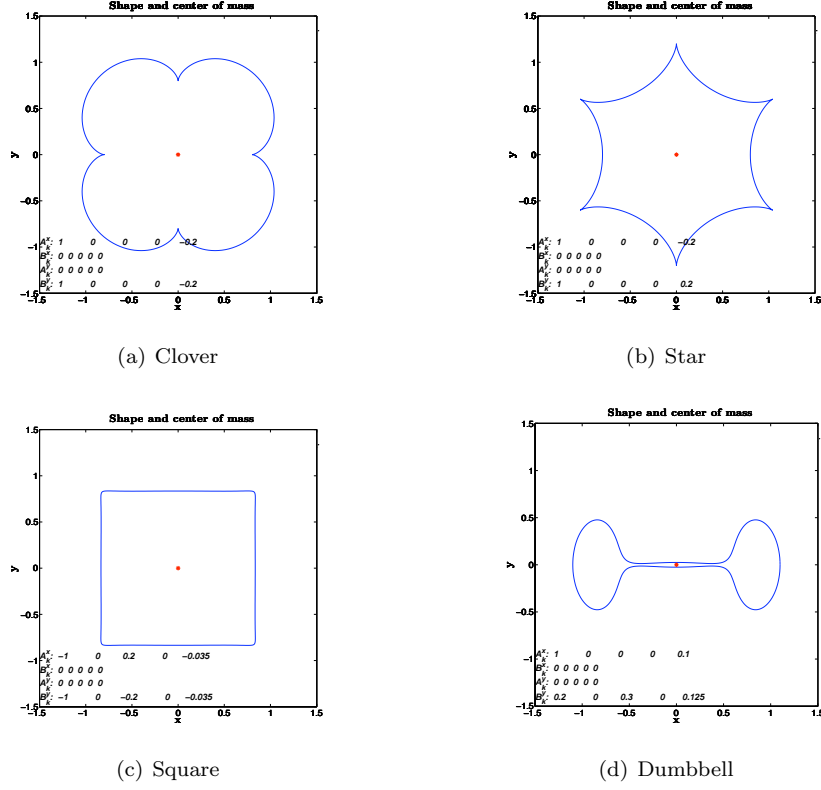


Figure 2.5: Some shapes and their coefficients. Figure (a) displays a clover-like structure with highly curved cusps. All coefficients are zero except $A_1^x = 1$, $A_5^x = -0.2$, $B_1^y = 1$ and $B_5^y = -0.2$. Compared to Figure (b) that shows a starlike shape, the only difference is the sign of B_5^y , making it obvious that only using the 5th coefficients (besides of the 1st ones) can lead to a 4-fold symmetry or a 6-fold symmetry - depending on the combination of their sign. The nearly rectangle contour plotted in Figure (c) illustrates quite straight lines and sharp edges by exerting only 6 coefficients ($A_1^x = -1$, $A_3^x = 0.2$, $A_5^x = -0.04$, $B_1^y = -1$, $B_3^y = -0.2$ and $B_5^y = -0.04$). The dumbbell shape in Figure (d) is an example of a non-selfintersecting, non-starlike outline ($A_1^x = 1$, $A_5^x = 0.1$, $B_1^y = 0.2$, $B_3^y = 0.3$ and $B_5^y = 0.125$) and coevally reflects the observed shapes (see Figure 1.1 and 1.4).

Symmetry

In usual Fourier series, symmetry can only be achieved, by imposing some constraints on the coefficients. The same holds for the Fourier coordinate expansion. If we want to have axial symmetry to both the x - and the y -axis, we can use the symmetry of the 4th kind [8]. This means that the x coordinate has to obey $x(t + T/2) = -x(t)$ and additionally be an even function, whereas the y coordinate also has to obey $y(t + T/2) = -y(t)$ but supplementary be an odd function. See Figure 2.6 to validate these properties and assume $(t = 0) \hat{=} (x = 0)$. T is

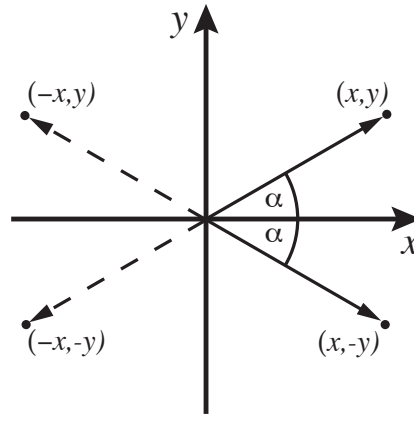


Figure 2.6: For axis-symmetry to both, x - and y -axis, it holds:
 $x(-t) = x(t) \rightarrow x$ is an even function.
 $y(-t) = -y(t) \rightarrow y$ is an odd function.
 We assume therefore $(t = 0) \hat{=} (y = 0)$ (If we assume $(t = 0) \hat{=} (x = 0)$, x is odd and y is even).
 $x(t + T/2) = -x(t)$ and $y(t + T/2) = -y(t) \rightarrow$ both are point-symmetric to $\mathcal{O}(0, 0)$.

the period and can be considered as the time needed for one revolution (provided the whole curve from its beginning to the end makes not more than one revolution). The angular frequency is defined as $\omega = \frac{2\pi}{T}$ and the notation therein should be changed to $\dots \cos(k \cdot \omega \cdot t)$ and $\dots \sin(k \cdot \omega \cdot t)$. But as T in our notation is set equal to 2π , nothing has to be modified. T just helps to get rid of the idea the parameter t being an angle. The coefficients for symmetry of the 4th kind then become

$$A_{2k+1}^x = \frac{4}{\pi} \int_0^{\pi/2} x(t) \cos[(2k+1) \cdot t] dt \quad k = 0, 1, 2, \dots \quad (2.12)$$

$$B_{2k+1}^y = \frac{4}{\pi} \int_0^{\pi/2} y(t) \sin[(2k+1) \cdot t] dt \quad k = 0, 1, 2, \dots \quad (2.13)$$

whereas the constraints are $B_k^x = A_{2k}^x = 0$ and $A_k^y = B_{2k}^y = 0$. The same symmetrical shape, but rotated to 90° can be achieved by assuming $(t = 0) \hat{=} (y = 0)$ and therefore x to be odd and y to be even. All coefficients then just have to be modified by swapping $x \leftrightarrow y$. This can always be done with axis-symmetric shapes. The only difference is the orientation of the curve (see section 2.3.2). Considering only axis-symmetry to the x -axis, we put away the point-symmetry ($x(t + T/2) = -x(t)$ and $y(t + T/2) = -y(t)$) and therefore the dashed arrows in Figure 2.6. The constraints now are $B_k^x = 0$ and $A_k^y = 0$ and the coefficients

calculate to

$$A_k^x = \frac{2}{\pi} \int_0^\pi x(t) \cos(k \cdot t) dt \quad k = 0, 1, 2, \dots \quad (2.14)$$

$$B_k^y = \frac{2}{\pi} \int_0^\pi y(t) \sin(k \cdot t) dt \quad k = 0, 1, 2, \dots \quad (2.15)$$

Now let us fix all values of the coefficients and only change their signs. Consider the case: $|A_1^x| = 1$, $|A_5^x| = 0.2$, $|B_1^y| = 1$ and $|B_5^y| = 0.2$, whereas all other coefficients are zero. Denote the signs of the four nonzero-coefficients in a quadruple according to the order specified.

$(+, -, +, -)$; $(-, +, -, +)$; $(-, +, +, -)$; $(+, -, -, +)$ all give the clover-like shape in Figure 2.5(a) and

$(+, +, +, +)$; $(-, -, -, -)$; $(+, +, -, -)$; $(-, -, +, +)$ lead to the same shape rotated by 45° (half of the angle of its 4-fold symmetry).

$(-, +, +, +)$; $(+, -, -, -)$; $(+, -, +, +)$; $(-, +, -, -)$ in contrast result in the starlike structure of Figure 2.5(b) and as expected

$(+, +, +, -)$; $(-, -, -, +)$; $(+, +, -, +)$; $(-, -, +, -)$ is the same star rotated by 30° .

If $|A_4^x| = 0.2$ and $|B_4^y| = 0.2$ are chosen to be nonzero instead of $|A_5^x|$ and $|B_5^y|$, the resulting 3-fold symmetric 'clover' will behave similar regarding the first and second set of quadruples but rotate to 60° and therein half of the angle of its 3-fold symmetry. The last and the second last set of quadruples now leads to a 5-fold-symmetric 'star' and consequently to a 36° rotation.

Slicing the nuclear envelope that will be described here in its middle section - which therein contains the long axis - leads to a 2-fold symmetric contour (neglect the orbital shape) and in any case there is a certain similarity to Cassini ovals or toric sections (when the torus is cut by a plane parallel to its rotational axis). Hence, instead of using common Cartesian coordinates one may think of using Bipolar coordinates [24] to describe the shape. But this should not simplify things, because in either way there are two variables to fix for defining a particular point. The transformation from Cartesian coordinates to Bipolar coordinates is unique when the x -axis-symmetric case is considered and hence only positive y -values for example.

2.1.4 Meaning of the coefficients

The interpretation of the coefficients is an interesting subject. A possible visualization are elliptic approximations to a contour based on the system of Ptolemy's epicycles like in [45]. For an interactive tool about epicycles see <http://physics.syr.edu/courses/java/demos/kennett/Epicycle/Epicycle.html> First, we consider curves in two dimensions. This is based on [49] and unpublished material of J. Howard (MPI-CBG, Dresden, Germany). Having a regular parametric representation $\vec{p}(t)$ like in equation (2.9), the time derivative calculates to

$$\vec{p}(t)' = \frac{d\vec{p}}{dt} = \lim_{\Delta t \rightarrow 0} \frac{\vec{p}(t + \Delta t) - \vec{p}(t)}{\Delta t} = \vec{t}(t)|\vec{p}'| = v(t) \cdot \vec{t}(t) \quad (2.16)$$

where $\vec{t}(t)$ is the unit tangent vector (pointing in the direction of travel) and $v(t)$ its magnitude (which can be seen as the speed). The faster the speed, the

more distant are subsequent 'points' when they are marked at a constant time interval while going along the curve. Thinking in terms of intensity or brightness: The slower the speed, the brighter the curve.

Herein lies the key advantage of such a parameterization: Additionally to defining a curve, it also comprises its intensity and therein includes the description of shapes with non-uniform intensity like they may occur in biological, stained samples due to some intrinsic gradient or samples with imperfect labeling.

Using a representation in terms of the arc length, we come to a natural representation, where $|\frac{d\vec{p}(s)}{ds}| = 1$. This means equidistant 'points' and therein uniformly distributed brightness of the curve. Inversely, curves of speed $|v| = 1$ are called 'parameterized by arc length' [31]. Note that if the arc length is defined as

$$s = s(t) = \int_{t_0}^t \left| \frac{d\vec{p}}{dt} \right| dt \quad (2.17)$$

then $\vec{p}(t(s))$ is also a natural representation and therefore no squeezing nor stretching of the curve occurs. The reparameterization $\vec{p}(s) = \vec{p}(t(s))$ then just yields

$$\vec{t}(s) = \frac{\frac{d\vec{p}(s)}{ds}}{\left| \frac{d\vec{p}(s)}{ds} \right|} = \frac{d\vec{p}(s)}{ds} = \frac{d\vec{p}(t(s))}{ds} = \frac{d\vec{p}(t)}{dt} \frac{dt}{ds} = \frac{\frac{d\vec{p}(t)}{dt}}{\frac{ds}{dt}} = \frac{\frac{d\vec{p}(t)}{dt}}{\left| \frac{d\vec{p}(t)}{dt} \right|} = \frac{\vec{p}(t)'}{v(t)} = \vec{t}(t) \quad (2.18)$$

provided that the speed $v(t)$ is always positive ($\Rightarrow t(s)$ can be inverted $\Rightarrow \frac{dt}{ds}|_{t(s)} = [\frac{ds}{dt}|_{s(t)}]^{-1}$). Due to the positive v , the curves have the same orientation.

The average of a function f is defined as

$$\langle f \rangle_t = \frac{1}{b-a} \int_a^b f(t) dt \quad (2.19)$$

When we weight every increment of arc length by the intensity of the curve $i(t) = \frac{1}{v(t)} = \frac{dt}{ds}$ we get

$$\frac{1}{\Delta t} \int_{t_0}^{t_0+\Delta t} f(t) dt = \frac{1}{\int_{s_0(t)}^{s_0(t)+\Delta s} \frac{dt}{ds} ds} \int_{s_0(t)}^{s_0(t)+\Delta s} f(s) \frac{dt}{ds} ds \quad (2.20)$$

whereas, when we weight by both the brightness and the amount of arc length within the incrementing angle (and therefore by the overall curve material within that angle) we obtain

$$\frac{1}{\Delta t} \int_{t_0}^{t_0+\Delta t} f(t) dt = \frac{1}{\int_{\Theta_0(t)}^{\Theta_0(t)+\Delta\Theta} \frac{dt}{ds} \frac{ds}{d\Theta} d\Theta} \int_{\Theta_0(t)}^{\Theta_0(t)+\Delta\Theta} f(\Theta) \frac{dt}{ds} \frac{ds}{d\Theta} d\Theta \quad (2.21)$$

Now back to the coefficients of the Fourier coordinate expansion. For the zero order coefficients (also called the DC components) we have

$$A_0^x = \frac{1}{2\pi} \int_0^{2\pi} x(t) dt = \langle x \rangle_t \quad \text{and} \quad A_0^y = \frac{1}{2\pi} \int_0^{2\pi} y(t) dt = \langle y \rangle_t \quad (2.22)$$

so that they represent the coordinates of the center of mass. For a contour of uniform intensity, parameterized by the arc length it is also the center of the perimeter. For higher order coefficients it yields

$$A_k^x = \frac{1}{2\pi} \int_0^{2\pi} x(t) \cos(k \cdot t) dt = \langle x(t) \cos(k \cdot t) \rangle_t \quad (2.23)$$

$$B_k^x = \frac{1}{2\pi} \int_0^{2\pi} x(t) \sin(k \cdot t) dt = \langle x(t) \sin(k \cdot t) \rangle_t \quad (2.24)$$

and likewise for A_k^y and B_k^y . These higher order coefficients correspond to the closest fit in the least squares sense. For the best fit ellipse for example

$$\Omega^2(A_0^x, A_1^x, B_1^x, A_0^y, A_1^y, B_1^y) = \frac{1}{2\pi} \int_0^{2\pi} \left\{ [x(t) - A_0^x - A_1^x \cos(k \cdot t) - B_1^x \sin(k \cdot t)]^2 + [y(t) - A_0^y - A_1^y \cos(k \cdot t) - B_1^y \sin(k \cdot t)]^2 \right\} dt \quad (2.25)$$

is minimized. This gives an ellipse with minimal deviation to the curve, respecting the whole contour at the same time. If uniform intensity is expected and therein parameterization by arc length is used (see Figure 2.7), the best fit ellipse has not definitely to be traced out at constant velocity !

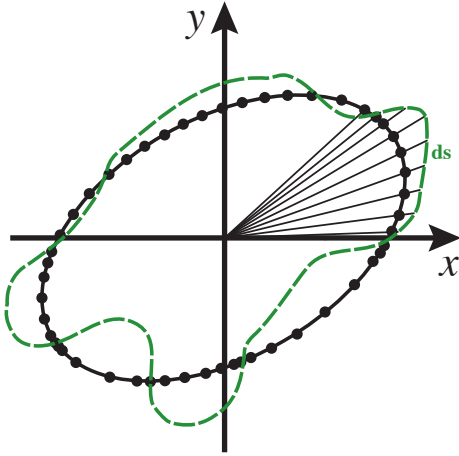


Figure 2.7: An arbitrary contour is plotted as a green, dashed line. It is parameterized by the arc length and therefore has uniform intensity and equidistant 'points'. The best fit ellipse according to equation (2.25) minimizes the overall deviations to the curve. Note that while the curve is traced out at constant velocity it is not necessarily the case for the ellipse. Remark: This figure is a thumbsketch, not a graph.

2.2 The 2-d-contour-explorer

By using the developed interface shown in Figure 2.8 one can get a good estimation how the different frequencies contribute to the appearance of a shape that is described by a Fourier expansion. The upper row of sliders represents the coefficients of the x -coordinate, the lower row the ones of the y -coordinate. Each row is divided in two groups of sliders. The group on the left-hand side provides the interface to manipulate the amplitudes of the first 5 harmonics of the cosine-part in the Fourier series in equations (2.10) and (2.11). The group situated to the right is connected to the harmonics of the sine-part. There is no

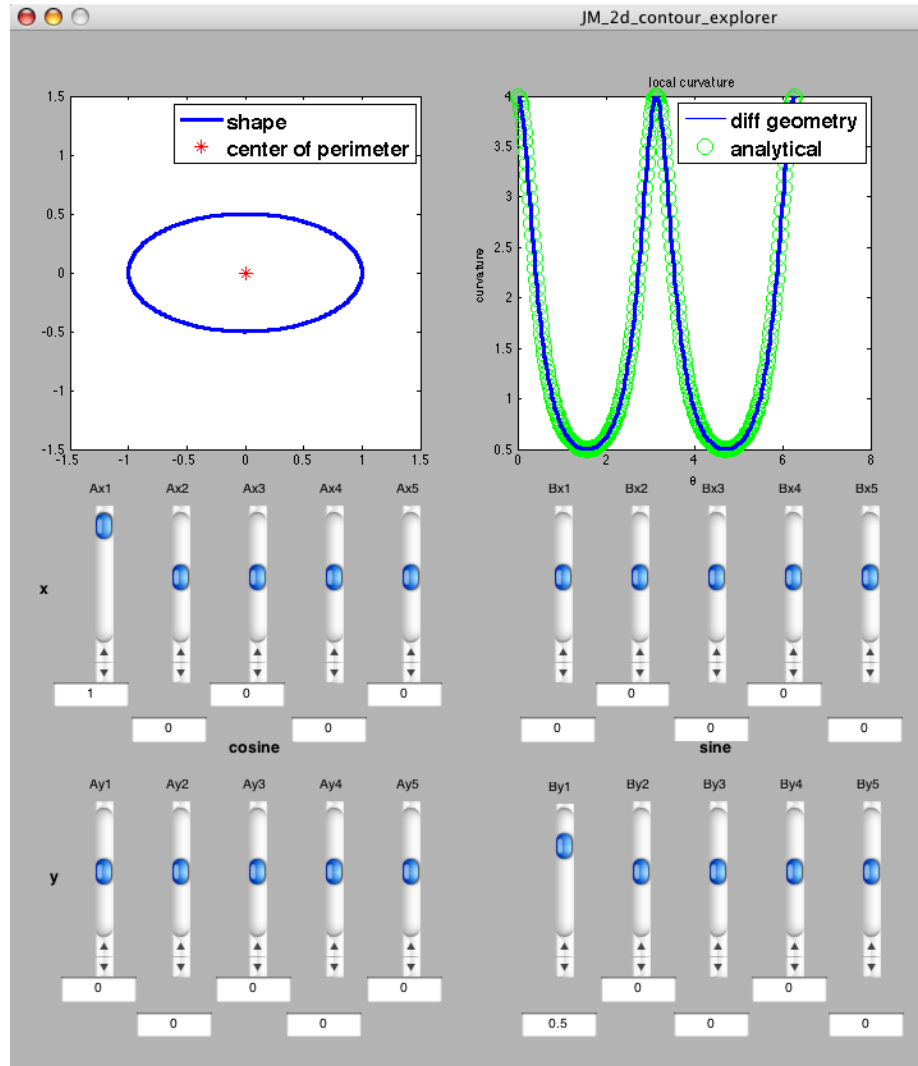


Figure 2.8: The interface to create a particular shape out of manipulating (slider or input field) the first 5 Fourier-coefficients both for x and y and for the cosine and sine in each case therein. On the graph to the left is plotted the actual shape and its center of mass corresponding to the slider values. The right-hand sided graph displays the local curvature of the actual shape drawn on the left - the blue line belongs to the program output, the green circles reproduce the analytical solution.

slider for the coefficient with subindex zero, because it would only dislocate the center of mass (as mentioned in section 2.1.4) and therefore only shift the whole shape without changing its appearance. Additionally the local curvature that corresponds to the shape of the sinistral graph is plotted in the dexter window. For basic shapes like the circle and the ellipse, the local curvature is compared to the analytic result (green circles).

2.3 Shape analysis

With our approach we can analyze shapes by tracing their boundary and redraw them using a particular set of coefficients. As we cut off high frequencies at some degree to avoid infinitive sums, only quite low frequencies will be used. This approximates the given shape to some order but represents a smoothed structure. The coefficients of the frequencies in the Fourier expansion are determined numerically by solving the matrix equation

$$\mathbf{A} \cdot \mathbf{c}_x = \mathbf{x} \quad (2.26)$$

for the \mathbf{c}_x array, where \mathbf{A} are the basis functions $(\cos(k \cdot t), \sin(k \cdot t))$, \mathbf{c}_x the coefficients (A_k^x, B_k^x) and \mathbf{x} the x -projection of the outline. The \mathbf{c}_y coefficients are calculated likewise. The \mathbf{c}_x and \mathbf{c}_y coefficients now equally represent the (smoothed) shape. Note that the shape is not uniquely associated to the set of coefficients found here, but there are other possible sets of coefficients that have the same resulting shape (as already mentioned in section 2.1.3). Generally the determination of the FS-coefficients is also called 'harmonic analysis' [8].

2.3.1 Decreasing amplitudes and truncation of the series

The amplitudes of the harmonics usually tend to decrease with increasing frequencies [26]. At a certain frequency order that depends on the specific shape, the coefficients are small enough to be negligible. To demonstrate this, the capital letter E will be analyzed. The (x, y) coordinates - one pixel corresponds to one unit - of a pixelated image of the letter are taken as original shape (see dashed lines in Figure 2.9(b), 2.11(a) and 2.11(b)). Using a different number of harmonics to do the analysis gives a different degree of adaptation. In the case of first order approximation the best fit ellipse is obtained (see Figure 2.9(a)). The solid lines in Figure 2.9(b) show the first harmonics modulated by the calculated amplitudes. Although the DC components of the series are zero as the center of mass is put to the origin of the represented coordinate system, the original and recalculated (x, y) coordinates are displaced due to better visibility - especially when taking more harmonics into account (see Figures 2.11(a) and 2.11(b)). Within the limits of only using the lowest frequency, the best fit is already visible in Figure 2.9(b). The frequency spectra of Figures 2.10(b), 2.10(d) and 2.11(d) correspond to the cross-labeled red shape to their left respectively. Comparing the first two it is obvious, that the amplitudes are the very same for each frequency and therein the truncation of a FS is equal to simplifying a shape or expressed in terms of frequencies just to remove high frequency-features of the contour. The decrease of the amplitudes with increasing order k is evident in Figure 2.11(d), making it reasonable that truncation does not matter in a pixelated image, as far as the truncation is chosen at an

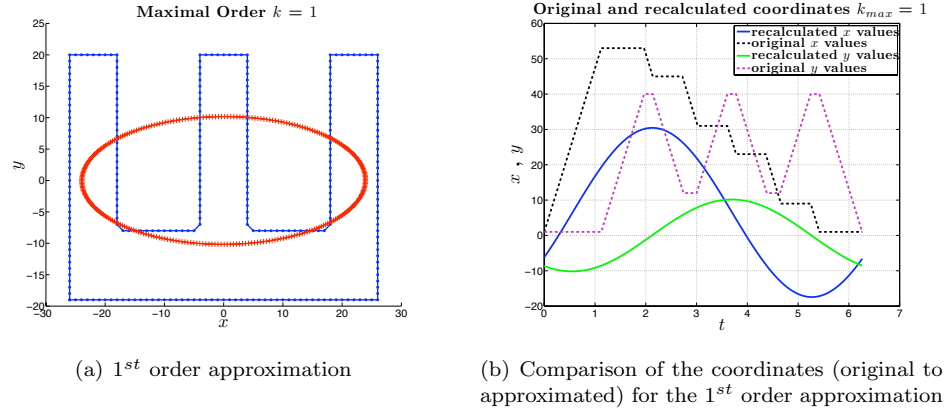


Figure 2.9: (a): The tilted letter E and the best fit ellipse yielded by solving the matrix equation (2.26) for the set of x - and y -coordinates starting counterclockwise in the lower left corner. Although the ellipse seems to be too small it is right, having in mind the negative y -value of some upper part and a relative big part of the curve near zero in x -direction. (b): The dashed lines are the x - and y -values of the letter E plotted over the parameter t (natural representation). The solid lines display the 1st harmonic representation. They are dislocated in y -direction for better visibility.

appropriate high order. Amplitudes much smaller than one should have no effect to the pixelated shape. Also frequencies with a wavelength smaller than a pixel should definitely not be considered. As we implicitly assume some degree of smoothness for the nuclear membrane, the truncation can be done even earlier (at lower frequencies). A way of thinking about the different harmonics of the truncated FS is similar to Ptolemy's epicycles (mentioned in section 2.1.4). As Kuhl and Giardina [27] already showed, the points (x, y) all have elliptic loci. So the truncated FS can be seen as the additive accumulation of rotating phasors, each in proper phase relationship. Each rotating phasor has its origin on the elliptic locus of the previous one and rotates k times faster than the first harmonic (k being its harmonic number). The resulting shape then is drawn by the end of the phasor of highest respected order. A different starting point on the contour does not change the elliptic loci but the phasors will take a different orientation [45]. Figure 2.12 shows a sketch of the situation. How the different elliptic loci play together to produce the resulting particular shape is visualized at <http://lmb.informatik.uni-freiburg.de/lectures/mustererkennung/WS0405/FourierDemo/fourdem.html> and choosing a different number of harmonics clearly shows what the truncation of the FS causes.

2.3.2 Calculating the 2-dimensional properties

Calculation of the properties is an important point, because it allows to draw conclusions about more general features of a particular shape and they are the basis for more advanced calculations. Given a set of coefficients the local curvature, the area and the contour length are easily calculated as they depend only on the first and second derivatives as well as on the x and y values itself.

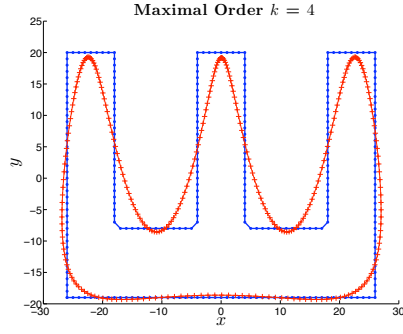
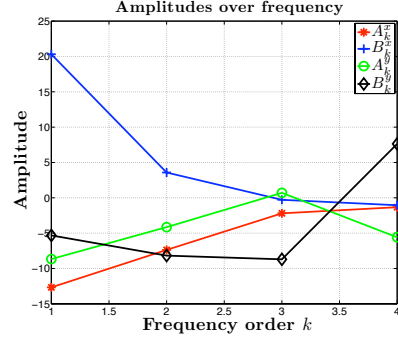
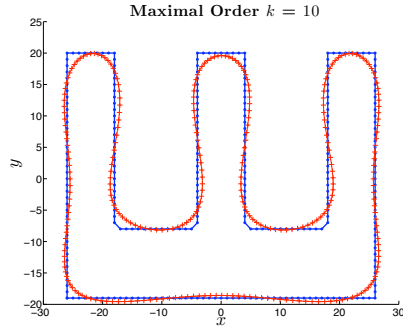
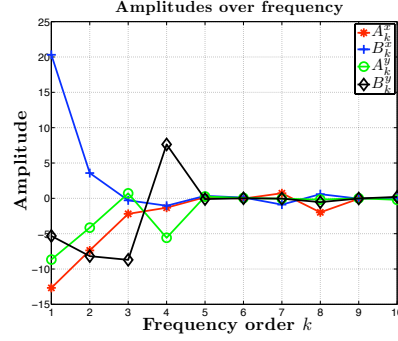
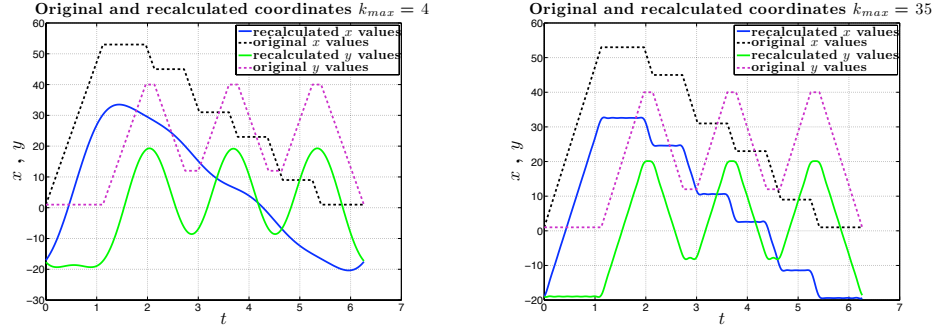
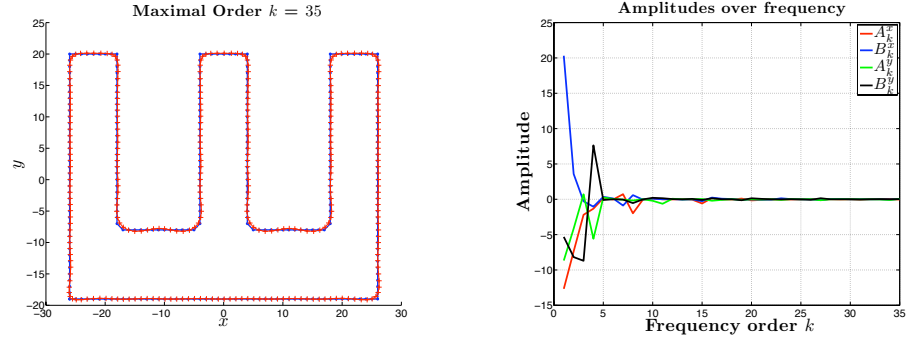
(a) 4th order approximation(b) Spectrum of the 4th order approximation(c) 10th order approximation(d) Spectrum of the 10th order approximation

Figure 2.10: (a) and (c) show the gradually better adaption to the given shape, including an increasing number of harmonics. Note the non-uniform distribution of the approximation compared to the uniform original shape. (b) and (d) show the corresponding spectra of the approximations in (a) and (c) respectively. The first 4 orders in (b) and (d) are the very same, showing in (d) the usual decrement of amplitudes of higher order frequencies [26]. The additionally incorporated higher frequencies in (d) are responsible for finer adaption to the original. The zero-order amplitudes are not displayed as the center is chosen to be $\mathcal{O}(0,0)$.



(a) Comparison of the coordinates (original to approximated) for the 4th order approximation

(b) Comparison of the coordinates for the 35th order approximation



(c) 35th order approximation

(d) Spectrum of the 35th order approximation

Figure 2.11: (a) and (b) illustrate the increasing adaption of details by higher harmonics. The crude main features are already visible by 4th order approximation. Like in Figure 2.9(b), the original and approximated curves are displaced against each other. (c): The 35th order approximation nearly shows no difference to the original shape. (d): Obvious decreasing of the amplitudes by increasing k . Here it becomes visible that frequencies higher than 30 can be neglected, as they only try to match the pixel-to-pixel digital structure of the object, which is probably not an important feature of the real object.

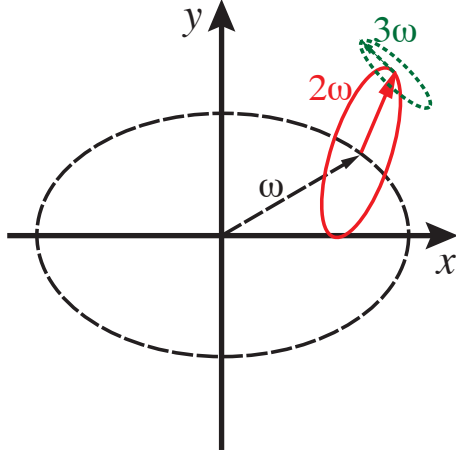


Figure 2.12: The first three rotating phasors that represent the first three harmonics: The black, dashed elliptic locus is the 1st harmonic. The red, solid ellipse represents the 2nd harmonic, that rotates with double the frequency of the first one. The green, dotted locus with three times the frequency of the first one acts for the 3rd harmonic. Letting rotate all phasors, the end of the highest considered order will trace out the contour. Given a determined shape, the same elliptic loci are used regardless of the starting point on the contour. The only difference will be their orientation [45].

Local curvature

The local curvature κ in 2 dimensions equals $\frac{1}{r(t)}$, where $r(t)$ is the radius of a circle that snuggles itself to the curve at the considered point (the so called osculating circle). In other words the curvature is the derivative of the tangent angle ϕ with respect to the arc length $\kappa = \frac{d\phi}{ds}$. Using differential geometry calculations for a curve given by Cartesian parametric equations $x(t)$ and $y(t)$, the curvature is calculated to

$$\kappa = \frac{x'y'' - y'x''}{(x'^2 + y'^2)^{3/2}} \quad (2.27)$$

where $x' = \frac{dx}{dt}$ and $x'' = \frac{d^2x}{dt^2}$, respectively for y . This is done using the identity

$$\tan \phi = \frac{dy}{dx} = \frac{\frac{dy}{dt}}{\frac{dx}{dt}} \equiv \frac{y'}{x'} \quad (2.28)$$

and therein

$$\frac{d}{dt}(\tan \phi) = \sec^2 \phi \frac{d\phi}{dt} = (1 + \tan^2 \phi) \frac{d\phi}{dt} \equiv \frac{x'y'' - y'x''}{x'^2} \quad (2.29)$$

Note that 'time parameterization' is used and therefore

$$\kappa = \frac{d\phi}{ds} = \frac{\frac{d\phi}{dt}}{\frac{ds}{dt}} = \frac{\frac{1}{1+\tan^2 \phi} \frac{x'y'' - y'x''}{x'^2}}{\sqrt{x'^2 + y'^2}} = \frac{x'y'' - y'x''}{(x'^2 + y'^2)^{3/2}} \quad (2.30)$$

For the 3-dimensional, rotational symmetric shape there are the two principal curvatures, one along the meridians κ_m and - perpendicular to it - the second one along the parallels of latitude κ_p , both defined as in [15]. (More details in section 2.5.1)

Area, perimeter and center of perimeter

Area: For the parametrically specified curve, the area calculates to

$$A = \frac{1}{2} \int_0^{2\pi} (xy' - yx') dt \quad (2.31)$$

assuming that the parameter t ranges from 0 to 2π . This equation is derived by the help of *Green's theorem* or the isoperimetric inequality [19] and therefore we do have a signed area and have to travel around the region such that it lies on the left of our way to get a positive result. In the special case of having only first-harmonic amplitudes, the area becomes the simple form $A = \pi(A_1^x \cdot B_1^y - B_1^x \cdot A_1^y)$. Here it becomes obvious: When we put $B_1^x = A_1^y = 1$ and $A_1^x = B_1^y = 0$, the resulting circle will be drawn clockwise. The enclosed area is on the right side of the way and therefore is denoted negative. Areas of curves with self-intersections must be computed as a sum of absolute values of the areas of their components and should be excluded here.

Perimeter: The arc length is defined as the length along a curve (see also 2.1.4) and so the perimeter here calculates to

$$L = \int_0^{2\pi} \sqrt{x'^2 + y'^2} dt \quad (2.32)$$

because it is just the sum of the differential arc length $ds = \sqrt{dx^2 + dy^2}$ in infinitesimal steps from the starting point along the curve back to its origin ($\hat{=}$ $t = 0 \dots 2\pi$). Note that this integral (like any property of a curve) is independent of the parameterization [67] (always assuming that a simple regular curve is considered and hence excluding self-intersection).

Center of perimeter: As it is calculated as a weighted sum over the way along a curve, its x-component is

$$\bar{x} = \frac{\int_0^{2\pi} x(t) \sqrt{x'(t)^2 + y'(t)^2} dt}{L} \quad (2.33)$$

where L is the perimeter length calculated in equation (2.32). The \bar{y} component is calculated correspondingly.

2.3.3 Program testing

To be sure the programed code works properly and calculates the right properties, it is crucial to test the written programs by comparing its results with the analytic solution of well known shapes. Therefore we compare the area, the perimeter length (see Table 2.2) and the local curvature with the expected values derived by the well known formulas $A = \pi r^2$ for the area and $L = 2\pi r$ for the perimeter length of a circle as well as the local curvature. Let be $r = 1$ for the unit circle, then the local curvature is constant and equals 1 for any point on the circle. Two different methods are used for the calculation of the perimeter, one using differential geometry (showed in equation (2.32)), the other one summing up the polygon parts of adjacent points (Archimedes calculated

Circle ($r = 1$)	program output	analytic solution
Area	3.1416	3.1426
Perimeter (diff geometry)	6.2832	6.2832
Perimeter (point to point)	6.2831	6.2832

Table 2.2: Comparison of the program output with the analytical result for the circle

π up to the 2^{nd} significant by a polygon with 96 points approximating a circle. Using an increasing number of steps, we got the same result for summing up the polygon parts with our program and by ≈ 100 (equally spaced) steps and above, the length converged to $2\pi r$.

Additionally we are looking on a non-uniform shape with known analytical solutions like the ellipse. Here the area is to be $A = \pi ab$, with 'a' being the semimajor axis and 'b' being the semiminor axis. For the perimeter length we have to use an approximation to avoid the infinite sum

$$L = \pi \cdot (a + b) \cdot \sum_{n=0}^{\infty} \binom{n}{k}^2 \cdot h^n \approx \pi \cdot (a + b) \cdot \left(1 + \frac{1}{4}h + \frac{1}{64}h^2 + \frac{1}{256}h^3 + \dots\right)$$

where $h = \left(\frac{a-b}{a+b}\right)^2$. For $a = 1$, $b = 0.5$ it is reasonable to neglect terms of the order $\mathcal{O}(n > 3)$ if we are interested up to the 4^{th} significant, because the next term (for $n = 4$) would contribute $\approx 1.88 \cdot 10^{-5}$ to the sum on the right-hand side (Formula by *WolframMathWorld* or in a modified form by [8]). See Table 2.3 for the results.

Ellipse ($a = 1$, $b = 0.5$)	program output	analytic solution
Area	1.5708	1.5708
Perimeter (diff geometry)	4.8442	4.8442
Perimeter (point to point)	4.8441	4.8442

Table 2.3: Comparison of the program output with the analytical result for the ellipse

The center of perimeter differed in the worst case up to $\approx 10^{-5}$ from zero, what would be the expected value for symmetrical shapes like the circle and the ellipse (natural parameterization). The local curvature calculated by the program (blue line in the graph on the right-hand side in Figure 2.8) matches very well the analytically derived curvature (green rings in the graph on the right-hand side in Figure 2.8) that is gained by

$$\kappa = \frac{a \cdot b}{[b^2 \cos^2(t) + a^2 \sin^2(t)]^{3/2}}$$

which is derived by plugging $x = a \cdot \cos(t)$ and $y = b \cdot \sin(t)$ into equation (2.27).

2.3.4 The Elephant

In the spring of the year 1953 - during a meeting with Freeman Dyson - Enrico Fermi said [21]: "I remember my friend Johnny von Neumann used to say, with

four parameters I can fit an elephant, and with five I can make him wiggle his trunk.” Wei [73] used a least square Fourier sine series to do this, but required about 30 terms. With the method described here and the outline of a hand drawn elephant we can fulfill Fermi’s quotation ! Analyzing the picture in Figure 2.13 A) and eliminating amplitudes less than 5.9, we get the ‘raw’ spectrum. Slightly modifying the remaining amplitudes leads to the spectrum seen in Figure 2.13 B). By applying these coefficients to complex numbers, we have the equivalent of an elephant contour coded in a set of 4 complex parameters. The 5th parameter can be used to let the trunk wiggle (see Figure 2.13 C)). More precisely, the real part of the 5th parameter is assigned to a ‘wiggle parameter’ that sets the x -component where the trunk is supposed to be attached to the body. Its imaginary part is used to determine the coordinates of the eye (both x - and y -component). The parameters are compiled in Table 2.4 (for details see Legend).

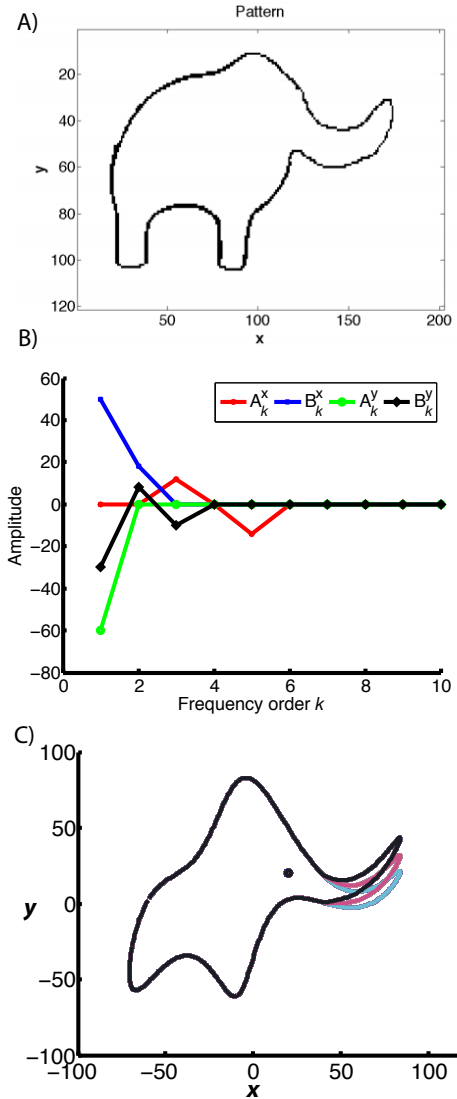


Figure 2.13:

A) This outline of an elephant is used as the pattern that is analyzed with the algorithm mentioned in section 2.3 ‘Shape analysis’ to get the coefficients. As explained in section 2.3.1 ‘Decreasing amplitudes and truncation of the series’ it is reasonable to neglect coefficients that contribute very little compared to the major amplitudes, which will lead to a smoothed shape like in Figure 2.13 C).

B) The frequency spectrum of the shapes seen in Figure 2.13 C). All high frequencies from the original picture in Figure 2.13 A) are suppressed as well as all frequencies whose amplitude is smaller than 5.9. Small modifications are then applied to the remaining ones. The frequency order k corresponds to the summation index in equations (2.10) and (2.11).

C) 3 different stages of the wiggling trunk. 4 parameters are used to determine the shape. The 5th is used for the wiggling and the position of the eye.

The resulting shape is quite schematic and cartoon-like, but still recognizable as an elephant.

Parameter	real part stands for	imaginary part stands for
$p_1 = -60 - 30i$	$A_1^y = -60$	$B_1^y = -30$
$p_2 = 8 - 10i$	$B_2^y = 8$	$B_3^y = -10$
$p_3 = 12 - 14i$	$A_3^x = 12$	$A_5^x = -14$
$p_4 = 50 + 18i$	$B_1^x = 50$	$B_2^x = 18$
$p_5 = 40 + 20i$	wiggle coefficient = 40	$x_{eye} = y_{eye} = 20$

Table 2.4: The 5 parameters $p_1 - p_5$ that encode the elephant including its wiggling trunk and what their components stand for. The notation corresponds to that used in equations (2.10) and (2.11), whereas the wiggle coefficient is the x -value of the body + trunk-attaching-line.

2.4 Application to confocal images

In case of real data images, the contours are mostly not that well defined as is an artificially designed image or even a binary image. The crucial question is to find the borders of an object in a way that is robust against noise and respects its properties, such that a best adaption is achieved without falling into pixel artefacts. This is usually done by active contours ([23], [42], [58]) where the gradient and energy functionals are being used. We in our case use the χ^2 -method and the bending energy to calculate the position of the membrane. So we use intrinsic knowledge about the smoothness of the nuclear envelope for determining a pareto optimality [10], [13] by computing the L-curve.

2.4.1 From the coefficients to the shape

Having a given set of coefficients, we can mimic a confocal image by translating the coefficients to a contour and then convolve it with a PSF and adding Gaussian noise. The two latter things just simulate what happens in the microscope. The natural way of thinking to design a curve in a pixelated world is to take the contour and to cover it with a tiny mesh (several times tinier than the pixel mesh). Every box of this tiny mesh that is intersected by the curve is assigned the value 1, all the other boxes become 0. This creates a binary image. Then binning is applied to regain the original number of pixels. The pixels then have different values according to the length of curve material within the specific pixel. This is to be convolved with the PSF.

Another - more analytical - idea is just to convolve the cuve with the PSF. Numerically this can be imagined as follows: A symmetric 2-dimensional Gaussian centered at one particular point of the curve. Then integration over the pixel containing this point and also integration over every single pixel in a reasonable neighborhood ($\approx 4\sigma$) of the center-pixel is applied and the calculated values are assigned to the corresponding pixels. When this is done for every point of the curve, we get the desired broadened contour.

If we want to create a uniformly distributed intensity, we have to be aware that

the strength S of the line impulse [6] of a function $f(x, y)$ is

$$S = \left| \frac{\partial f}{\partial \vec{n}} \right|^{-1} = \frac{1}{|\text{grad } f|} \quad (2.34)$$

and can be interpreted as the intensity $i(t) = \frac{1}{v(t)}$ defined in section 2.1.4. So either we have to parameterize by arc length or to multiply by $v(t)$. In the latter case the points of a curve primarily of uniform intensity but probably different distance to its neighbors become values corresponding to the length of its tangent vector. Now the convolution with the PSF delivers the broadened contour of uniform intensity. This method will be preferred, as it is computationally less expensive than using a finer meshsize (see above) and more accurate because no binning is needed.

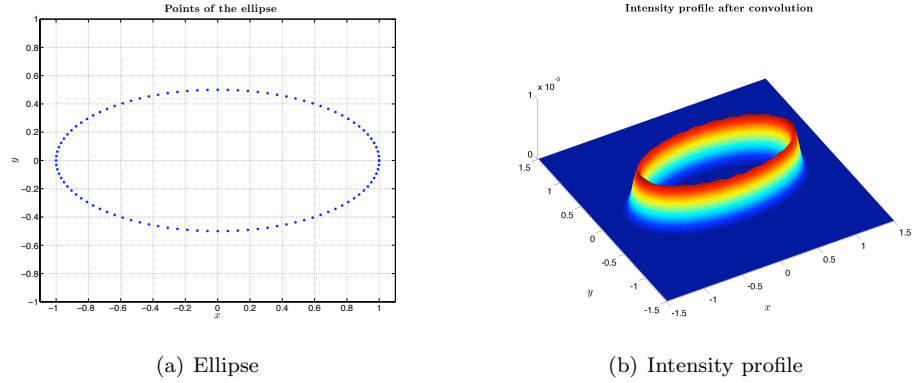


Figure 2.14: (a): The ellipse represented here is not of uniform intensity, but twice as intense at $y = 0$ (semimajor axis) as it is at $x = 0$ (semiminor axis). Every single point however is of the same intensity as all the others. (b): After multiplying the intensity of every point by $v(t)$ and convolving the result with a PSF, the displayed intensity profile is obtained. The intensity is visualized in z -direction. Now the ellipse is of uniform intensity.

As an example consider the ellipse with semimajor axis $a = 1$ and semiminor axis $b = 0.5$ in Figure 2.14(a). The elliptical line impulse [6] and therefore the intensity is twice as great at the ends of the major axis as it is at the end of the minor axis (and equally: Neighboring points are twice as dense). Secondary this reflects the fact that the radial beam coats the same area in a time interval Δt (this is proven using Heron's formula [8] to calculate the area) and the only difference to Keplers third law is that the beam originates in the center instead of originating in one focus of the ellipse. By multiplying every point (that all have the same intensity) by $v(t)$ before convolving with the PSF we get the uniformly distributed intensity of Figure 2.14(b). For a better visualization, the intensity is plotted in z -direction.

2.4.2 From the shape to the coefficients

Principally, the way to get the coefficients of a contour is described in section 2.3, but there we assumed a well defined contour. In images like the used confocal

images of the *S. pombe* nucleus, the boundaries are not so well defined. To get a connection between the shape and the coefficients, the 'artificial' image $\mathbf{I}_{\text{synth}}$ with known coefficients that we create using the method described in the previous section is compared with the data image \mathbf{I}_{data} . This is done calculating

$$\chi^2 = \sum_{i=1}^N [\mathbf{I}_{\text{data}} - \mathbf{I}_{\text{synth}}(A_k^x, B_k^x, A_k^y, B_k^y)]^2 \quad (2.35)$$

what is a pixelwise subtraction of the two images, and summing up the squared differences. The $\mathbf{I}_{\text{data}}, \mathbf{I}_{\text{synth}}$ are matrices and the summation index i is going over all matrix elements. χ^2 therefore is a measure for the similarity of the two (grayscale) pictures and called the 'merit function'. Altering the coefficients leads to a different image and therein a different χ^2 . The more similar the pictures, the smaller is χ^2 and its minimization yields the best-fit-parameters. These hereby found set of coefficients then reproduce the given shape. Minimization of χ^2 though is equivalent to the maximization of the likelihood of the model that is optimized, because the probability of the data set is the product of the probabilities of each point [60], so that here it is

$$P = \prod_{i=1}^N e^{-[\mathbf{I}_{\text{data}} - \mathbf{I}_{\text{synth}}(A_k^x, B_k^x, A_k^y, B_k^y)]^2} \quad (2.36)$$

Maximizing this is equivalent to maximizing its logarithm or equally minimizing the negative of its logarithm, what leads to equation (2.35).

Data image enhancement

Even though we do have several sections of the nucleus in z -direction, there is no maximum projection applied, because this accumulates also the noise and as different z -stacks have different radii will result in a less accurate determination of the position of the membrane. The middle section is selected by eye. To make it more easy for the algorithm to minimize χ^2 , the noise in the data image is suppressed. This is done in two similar steps. First, the 3-by-3 neighborhood, then the 5-by-5 neighborhood of every pixel is examined if there are a specific number of pixels below a certain threshold (which is derived by analyzing the histogram). In the positive case, the accordant pixel is set to zero. As it is very unlikely to fulfill the conditions near the labeled membrane, there is no loss of information, but most of the noise will be erased. The best results for smoothing the hereby acquired picture were obtained by using a Gaussian filter. The smoothing makes it easier for the minimization routine (see next section) to find the minimum. Note that the smoothing does not change the center of the pattern, it just smears the intensity.

Downhill-simplex- and interior-reflective Newton- method

The problem that we have to solve is to find the minimum of a multivariable function, so that we have an unconstrained nonlinear optimization. In **MATLAB**[®] the best two functions to perform $\min_x f(x)$ are **fminsearch** and **fminunc**. The first uses the simplex search method of Lagarias et al. [46] and is a direct search method that does not use gradients. It just oozes downhill in the parameter

space until it encounters a minimum (at least a local one). The second is based on the interior-reflective Newton method described in [11] and either needs a gradient provided or locally calculates the gradient. In both methods and even generally in optimization problems, the main difficulty is not to fall into a local minimum, when searching for a global one. Starting the algorithm already close to the global minimum by providing an appropriate set of initial parameters is very helpful (see next section).

No matter which method is used, simply using equation (2.35) and trying to minimize χ^2 will rarely lead to success in our case. To be able to compare the two images we have to 'normalize' or scale one of them. This must be done by no other method than calculating a scaling factor γ that minimizes the norm of the vector $\vec{s}\gamma = \vec{d}$ (and therefore its length), so that

$$\gamma = \min \left(\sqrt{\sum_{i=1}^N (s_i \gamma - d_i)^2} \right) \quad (2.37)$$

where d_i are the pixel-intensities of \mathbf{I}_{data} , s_i the pixel-intensities of $\mathbf{I}_{\text{synth}}$ and N the overall number of pixels in the images. In other words, γ is the solution to the system of equations $\vec{s}\gamma = \vec{d}$ in the least squares sense. Equation (2.35) then has to be modified to

$$\chi^2 = \sum_{i=1}^N [\mathbf{I}_{\text{data}} - \gamma \cdot \mathbf{I}_{\text{synth}}(A_k^x, B_k^x, A_k^y, B_k^y)]^2 \quad (2.38)$$

A good starting guess

To guarantee a successful result, the initial guess should be very close to the sought contour or at least not too far away. This is best done automatically. The method should provide the initial set of coefficients for a confocal image of the nucleus in any particular stage during the division. Images obtained by the procedure explained in section 'Data image enhancement' (see above) are considered. Depending on the quality two different methods were used. The easier one is thresholding, neglecting small objects and analyzing the resulting binary image following section 2.3. The initial contour then is very likely to the outer edge of the shape in the image. The other one rotates the image horizontally (if necessary), calculates the center of the structure, divides the image at the calculated x -centroid into two pictures (left and right) and again calculates the center of the structure in the two pictures individually. The two parts are treated likewise and so the following steps are explained only for one part. The centroid becomes the origin $\mathcal{O}(0,0)$ of a jet that scans the image radial-like to get an intensity profile. A Gaussian profile is fitted to every single intensity profile and its center is stored as $\vec{r}(\Theta)$. The polar notation is transformed to cartesian coordinates (\mathbf{x}, \mathbf{y}) and then put together with the corresponding (\mathbf{x}, \mathbf{y}) of the other part. The combined (\mathbf{x}, \mathbf{y}) now represent a closed contour that lies in the middle of the broad fluorescent structure seen in the image. These \mathbf{x} and \mathbf{y} arrays are plugged in the matrix equation (2.26) to get the desired initial coefficients. This is computationally not expensive and the preferred method. In case of the interior of the shape not clearly belonging to the background (and $\mathcal{O}(0,0)$ therefore not close to zero intensity), the first method is used.

Program testing

To assure that - in principle - the algorithm works, an artificially created image is used as a \mathbf{I}_{data} . Hence, we know exactly all the amplitudes of the coefficients and can compare them to the ones delivered by the minimization process. The initial guess for the coefficients is chosen to be quite far away from the objective ones. Figure 2.15 shows the iterative process of minimizing χ^2 and therein the convergence of the initial coefficients to their target (which is an ellipse, as all objective coefficients except B_1^x and A_1^y are chosen to be zero). The first three harmonics are used, so the minimization is done in a 12 dimensional parameter space. To estimate how far away the initial guess can be from the objective

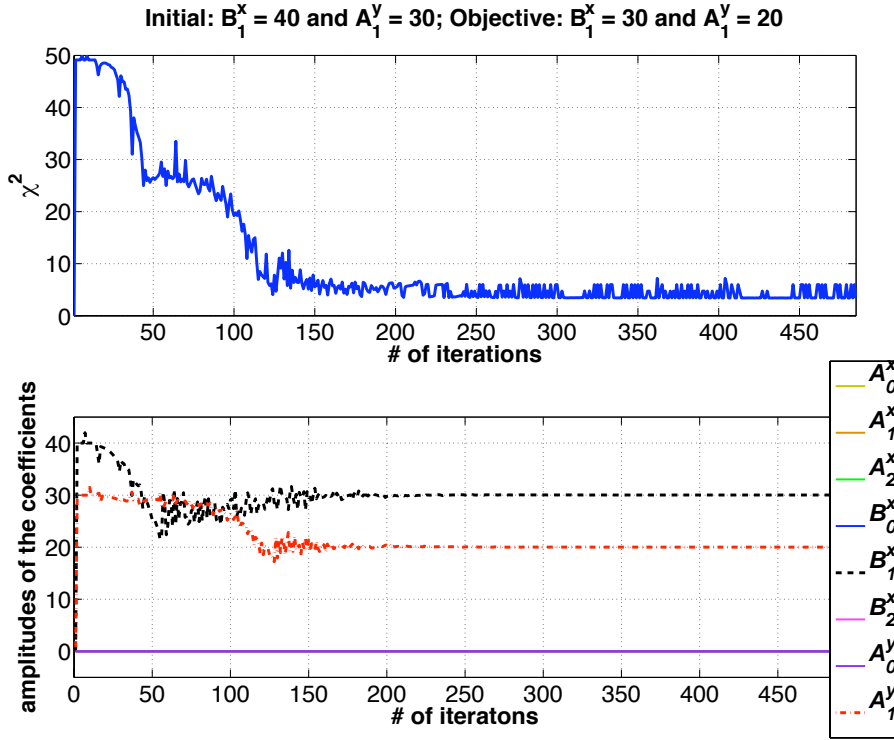


Figure 2.15: χ^2 (top) and the corresponding amplitudes (bottom) of the used coefficients are plotted over the iterations of the minimization procedure. An artificial image (of an ellipse with semiaxes $B_1^x = 30$ and $A_1^y = 20$) is used as the data image. The initial guess for the semiaxes ($B_1^x = 40$ and $A_1^y = 30$) converges towards the objective values. The three first harmonics are used but only 8 of the used 12 coefficients are displayed in the legend, as most of them do not depart much from zero.

set of coefficients, an exemplary real data image (nearly circle-shaped) is taken and different combinations of initial parameters are fed to the minimization algorithm. It turned out that for the real data it is highly crucial to have a good initial set, as the energy landscape is more jagged.

2.4.3 Bending energy and the L-curve

In addition to the visual information that we get out of the image, we do have extra knowledge about the nuclear membrane. It is assumed not to be too wrinkled, instead it is supposed to be quite smooth. In general, any bending of a membrane away from its preferred state requires energy, so that the membrane's resistance to bending stabilizes its shape [38]. Similar to the elastic energy of the surface in [15], the bending energy becomes

$$E_b = k_b \int_0^{2\pi} (\kappa - C_0)^2 dt \quad (2.39)$$

where k_b is the elastic modulus, κ the local curvature calculated in equation (2.27) and C_0 the spontaneous curvature [37] (the curvature in the natural, stress-free state of the contour). Therewith enters the area difference elasticity (ADE) model, that is connected to the spontaneous curvature model [20], because the effective spontaneous curvature (or equivalently an effective relaxed area difference) do not enter independently into the model [53]. The Gaussian curvature and the global curvature are not included due to the fact that they are constant for the integral over the closed 2-dimensional contour (Gauss-Bonnet theorem and 'turning tangent' [19]). In accordance to [14] the spontaneous curvature can be considered zero, so that we can finally denote the normalized bending energy as

$$E_b = \frac{1}{2\pi} \int_0^{2\pi} \kappa^2 dt \quad (2.40)$$

This can be used as a regularization term in our problem of χ^2 minimization (originally an ill-posed problem). The energy functional that has to be minimized now is

$$G(\mathbf{I}_{\text{data}}, A_k^x, B_k^x, A_k^y, B_k^y) = \chi^2(\mathbf{I}_{\text{data}}, A_k^x, B_k^x, A_k^y, B_k^y) + \lambda \cdot E_b(A_k^x, B_k^x, A_k^y, B_k^y) \quad (2.41)$$

where λ is the regularization parameter, that balances between the external image energy (χ^2) and the internal contour energy (E_b). In other words it weights the importance of smoothing the whole contour and the accuracy of fitting to the data image. The bigger λ , the smoother the shape and equivalently the lower E_b . The other way round: The smaller λ (and therein less important E_b), the closer the fit to the data and the more wrinkled the contour.

The same arguments as in [43] (computational affordable and incorporation of prior knowledge) account for using the L-curve method [36] to determine λ instead of minimizing the cross-validation or minimizing a Bayesian information criterion. Therefore the functional G is minimized every time, while λ is varied. Having reached the minimum for a particular λ , the logarithm of the achieved E_b is plotted over the logarithm of the corresponding χ^2 and the point is assigned the actual λ . The resulting 'curve' is L-shaped and is a trade-off between two quantities that both should be controlled. The λ -values in the corner of the L correspond to a transition between the two legs and the graphically determined optimal λ reflects the pareto optimality. Vogel [72] pointed out that the computed optimal λ is not the optimal parameter λ_{opt} , when the dimension of the

system increases significantly. This limitation to the L-curve is not met here, but in general the method tends to over-regularize and so to over-smoothing [35]. Additional attention has to be paid to the corner, when the regularization parameter is discrete (as in our case), because then the L-curve tends to cluster in a neighborhood of the corner [62]. Taking the image (processed by the

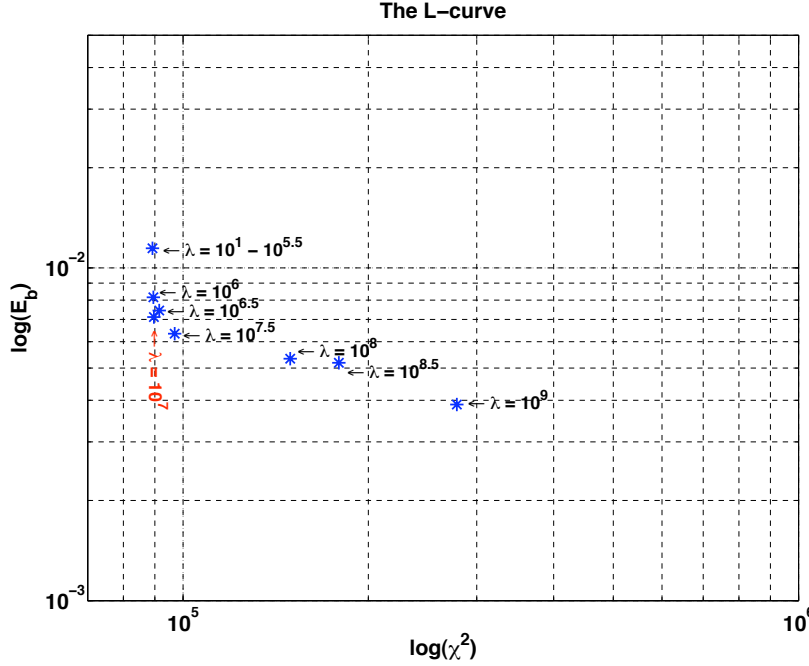


Figure 2.16: A double logarithmic plot of E_b against χ^2 . Every star is the result of minimizing G in equation (2.41) having a different, fixed λ value. The bottom, left image in Figure 1.4 is used as raw data image. The corner of the L-curve ($\lambda = 10^7$) is the optimal λ that respects both, the smoothness of the fit as well as closeness to the data. It is marked in red and displayed vertically. The 'horizontal' branch of the 'L' stands for the overregulated system, the vertical branch for the underregularized.

method described in section 'Data image enhancement') of the peanut-shaped nucleus and varying λ in equation (2.41) from 10^1 to 10^9 before minimizing G , we get the L-curve seen in Figure 2.16. The optimal λ is chosen to be $\lambda = 10^7$ (marked in red and written vertically), what expresses best the corner of the 'L'. The first point belonging to different λ values reflects the fact that the bending energy is weighted too lightly to play any role in the minimization of the energy functional G and the problem is not regularized. To recognize the influence of λ concerning the calculated shape see Figure 2.17. The resulting shape is overlaid with the analyzed image. If λ is too small (top), the contour sticks too much to the data, giving it an uneven appearance. Having a λ that is too high (bottom) results in a very smooth contour, but does not reflect the given data any more. Every additional curvature (more bending energy) would be too expensive for the energy functional. A further increase of λ would enforce a more and more circle-like contour. The chosen $\lambda = 10^7$ (middle) does both, smoothing the curve (and therefore respecting the additional knowledge about

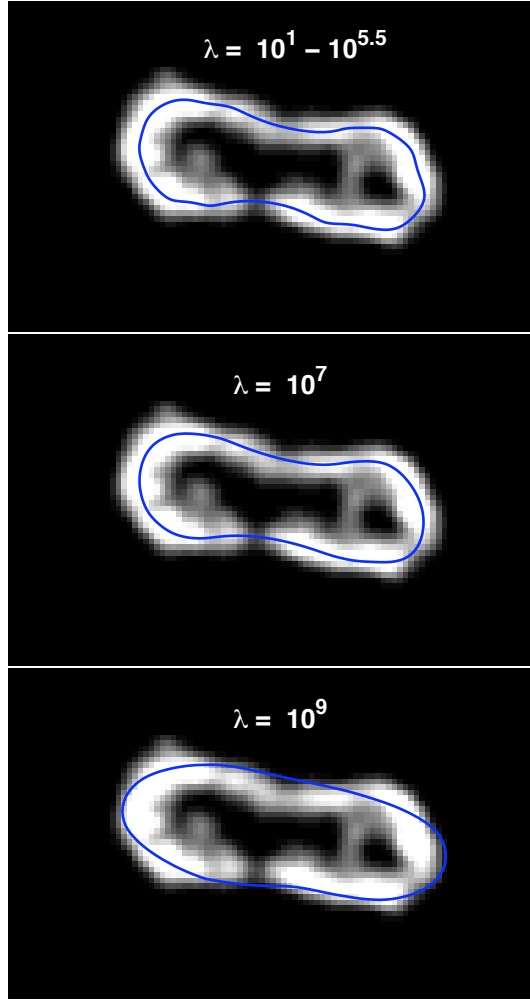


Figure 2.17: Overlay of the data image (after removing background and smoothing in the raw data image, see section 'Data image enhancement') and the resulting contour by minimizing the functional G in equation (2.41) for different, fixed λ values. For a wide range of small λ values there is no difference, because E_b is weighted too small and hence is not important compared to χ^2 . The problem is still unregulated and the contour fits best to the data (top), but has irregularities respective its curvature. $\lambda = 10^9$ (bottom) produces an over-smoothed shape, because of over-regularization. The bending energy has become very important and outweighs the closeness to the data. Only the best-fit parameter $\lambda = 10^7$ (middle) balances the two necessities and we have a smooth curve, that also reflects the data. The additional knowledge about the smoothness of the membrane is incorporated without disregarding the data.

the membrane) as well as reproducing the given data. This best λ value is then used to calculate the properties of the nucleus.

2.5 Extension to 3-d

The yeast nucleus is a 3-dimensional structure, so we should not restrict ourselves to 2 dimensions. Considering the space curve $\vec{p}(t)$ in three dimensions we get

$$\vec{t}(t) = \frac{\frac{d\vec{p}(t)}{dt}}{\left| \frac{d\vec{p}(t)}{dt} \right|} = \frac{\frac{d\vec{p}(t)}{dt}}{\frac{ds}{dt}}$$

as already showed in equation (2.18) and the curvature calculates to [32]

$$\kappa = \left| \frac{d\vec{t}}{ds} \right| = \frac{\left| \frac{d\vec{p}}{dt} \times \frac{d^2\vec{p}}{dt^2} \right|}{\left| \frac{d\vec{p}}{dt} \right|^3} = \frac{|\vec{p}' \times \vec{p}''|}{|\vec{p}'|^3} \quad (2.42)$$

where

$$\vec{p}(t)'' = \vec{t}(t)' = \frac{d}{dt} \vec{t}(t) = \kappa \frac{ds}{dt} \vec{n}(t) \quad (2.43)$$

and \vec{n} being the unit normal vector with

$$\vec{n} = \frac{\frac{d\vec{t}}{ds}}{\left| \frac{d\vec{t}}{ds} \right|} = \frac{\frac{d\vec{t}}{dt}}{\left| \frac{d\vec{t}}{dt} \right|} = \frac{1}{\kappa} \frac{d\vec{t}}{ds} \quad (2.44)$$

so that we have very important derivative relations (that are related to the Frenet formulas)

$$\frac{d\vec{p}(s)}{ds} = \vec{t}(s) \quad (2.45)$$

$$\frac{d^2\vec{p}(s)}{ds^2} = \kappa \vec{n}(s) \quad (2.46)$$

$$\frac{d^3\vec{p}(s)}{ds^3} = \kappa \vec{n}(s) + \kappa \left[\tau \vec{b}(s) - \kappa \vec{t}(s) \right] \quad (2.47)$$

$$\det \left(\frac{d\vec{p}(s)}{ds} \frac{d^2\vec{p}(s)}{ds^2} \frac{d^3\vec{p}(s)}{ds^3} \right) = \kappa^2 \tau \quad (2.48)$$

where $\vec{b}(s)$ is the binormal vector and τ the torsion [12]. A curve however is not enough, as we have to deal with surfaces and volumes. A surface can be described by its principal curvatures. The Gaussian curvature

$$K = \kappa_m \kappa_p = \frac{1}{R_m R_p} \quad (2.49)$$

is the product of the two principal curvatures (that is identical to the inverse product of the principal radii of curvature) and is an intrinsic feature. The Gauss-Bonnet theorem [19] for a compact, boundaryless 2-dimensional surface

$$\oint_{surface} K dA = 2\pi\chi \quad (2.50)$$

displays the fact that the integral of the Gaussian curvature over the surface is topologically invariant and means that all surfaces with the same number of handles or holes have the same integral Gaussian curvature. This is an interesting fact, because χ - the Euler-Poincaré characteristic [40] - does not at all depend on differential geometry, but puts a constraint on the curvature (what is a local property). Imagine a closed surface without holes like the sphere ($\chi = 2$). It can be arbitrarily deformed (for example to the dumbbell shape of the nucleus where also $\chi = 2$) but the total curvature is maintained, because implying an additional region of negative curvature will always be compensated by a corresponding positive integral curvature in other regions. This fact is used to assure the correctness of our computations. The mean curvature calculates to

$$H = \frac{1}{2}(\kappa_m + \kappa_p) = \frac{1}{2} \left(\frac{1}{R_m} + \frac{1}{R_p} \right) = \frac{1}{2}(R_m + R_p)K \quad (2.51)$$

and is used in the energy calculation of a membrane. The so called Helfrich-Canham free energy [14] is defined as

$$F_{H-C} = \oint_{surface} \left[\frac{k_b}{2} (2H)^2 - k_b 2HC_0 \right] dA \quad (2.52)$$

where k_b is the bending rigidity of the membrane and C_0 the spontaneous curvature (that characterizes the asymmetry of the membrane due to different inner and outer medium or lipid composition on the two sides). The model assumes the inner and outer NE as axisymmetric with a fixed interbilayer distance, connected via the NPCs. Minimizing this free energy, whereas respecting system-specific constraints and boundary conditions, we come to the equilibrium state of the membrane. The surface area A and the enclosed volume V (that are both calculated in the next section) can be considered constant analyzing one particular image of the nucleus during its division. They are denoted A_0 and V_0 respectively. These constraints can be implemented into equation (2.52) by the terms $\sigma A - pV$, where σ and p are the Lagrange multipliers [18]. The free energy therein becomes

$$F_{H-C} = \oint_{surface} \left[\frac{k_b}{2} (2H)^2 - k_b 2HC_0 + \sigma \right] dA - pV \quad (2.53)$$

The Lagrange multipliers have to be chosen in a way that the corresponding constraints ($A = A_0$, $V = V_0$) are fulfilled and their physical meaning will become the surface tension (σ) and the pressure difference between inside and outside the nucleus (p).

2.5.1 Calculating the 3-dimensional properties

For visualization of the 3-D appearance, we processed data acquired by the Zeiss UV (see section 1.3.3), using Imaris® (Bitplane AG) - software (threshold level 20/200, Gaussian filter width 0,2 μm). Figure 2.18 shows the nucleus during a stage similar to the one examined in section 2.4.3. To describe a figure in

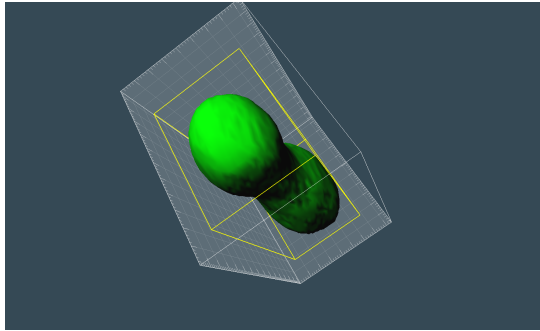


Figure 2.18: 3-d reconstruction of the nucleus during telophase, using data acquired by the Zeiss UV. Despite smoothing, the surface is still corrugated due to the irregular labeling of the membrane. Using the (aligned) rotating curve calculated by the L-curve (see section 2.4.3), we will get rid of these surface irregularities.

3 dimensions in terms of an expansion of basis functions we could use spherical harmonics (that are the 3-D equivalent to the FS) as Khairy [43] in his work about red blood cells or Brechbühler [7] describing closed surfaces. We then

could use for x , y and z the alike expansion separately

$$x(\Theta, \phi) = \sum_{l=0}^{\infty} \sum_{k=-l}^l C_{x_l}^k Y_l^k(\Theta, \phi) \quad (2.54)$$

where $\Theta = 0 \dots \pi$ and $\phi = 0 \dots 2\pi$. The $C_{x_l}^k$ are the coefficients and $Y_l^k(\Theta, \phi)$ the spherical harmonics [25].

But we take advantage of the rotational symmetry of the nucleus and assume the x -axis to be the rotational axis. Adapting Helfrich's notation [15] for shapes of rotational symmetry to our notation, we have: κ_m is along the meridians and κ_p along the parallels of latitude. But note that the surface normal generally lies not in the plane containing these parallels and the radius of curvature therefore is not the radius of these circles. In fact R_p is the distance between the two points where the surface normal penetrates the surface and where it intersects the x -axis. Helfrich's notation is changed from $z(x)$ to $y(x)$ and the axis of revolution is flipped from vertical to horizontal, which is equivalent to flipping $x \leftrightarrow y$. As the angle ψ still denotes the angle between the axis of revolution (here the x -axis) and the surface normal, we get $\kappa_p = \frac{\sin \psi}{y}$. In our case of having the parameterized curve $(x(t), y(t))$ defined above, this leads to

$$\kappa_p = \frac{|x'|}{|y| \sqrt{x'^2 + y'^2}} \quad (2.55)$$

Coevally this is the 2nd principal curvature. The 1st principal curvature (κ_m) is the curvature calculated in equation (2.27) on page 29. For accuracy we should mention that the usual calculation in the above equation is done by $-x'$ instead of $|x'|$ and equation (2.27) additionally is multiplied by $\text{sgn}(y)$. This would become important dealing with overhangs. However, we can keep the notation for convenience in calculating the Gaussian and mean curvature using the whole, closed contour instead of only $[0, \frac{T}{2}]$ (see section 2.5.2).

Volume of revolution

The rotational symmetry suggests to use cylindrical coordinates and we therefore calculate the volume of a rotational symmetric corpus by

$$V = \int_0^R \int_0^{2\pi} \int_{-L}^L r dr d\theta dl = \int_{-L}^L \pi R^2 dl$$

This is the intuitive way of summing up infinitesimal thin disks of radius $R(l)$. In our case this leads to

$$V = \pi \int_{x_0}^{x_1} [y(x)]^2 dx \quad (2.56)$$

as used in [8], where we are bound to have a unique function, so that we must exclude overhangs in x -direction. But as one can see in the exemplary images of Figure 1.1 this condition is not violated. The integration goes from the minimum x -value to the maximum x -value. (If one would integrate vice versa, the absolute value would have to be taken because of the negative dx .) Using

the parameterization this formula becomes

$$V = \pi \int_{t_0}^{t_1} [y(t)]^2 x(t)' dt \quad (2.57)$$

where t_0 and t_1 correspond to $x_0 = x(t_0)$ and $x_1 = x(t_1)$. Now, even overhangs can occur, because x' is of the opposite sign in the overhang-region and hence subtracts the volume between the overhang and the x -axis. Another possibility to calculate the volume is using the formula provided in [15], what leads to

$$dV = \pi y^3 \kappa_p (1 - y^2 \kappa_p^2)^{-1/2} dx \quad (2.58)$$

Surface of revolution

The area element of a curve rotated around the x -axis is $dA = 2\pi y ds$ (ds is the differential arc length calculated in section 2.3.2 'Area, perimeter and center of perimeter'). Replacing ds and using the integral over the parameter t gives

$$A = 2\pi \int_{t_0}^{t_1} y(t) \sqrt{x(t)'^2 + y(t)'^2} dt \quad (2.59)$$

for the entire surface area. Here there is also no constraint to avoid overhangs and t ranges from 0 to 2π (as stated calculating the perimeter in section 2.3.2), what automatically reflects the fact that we have a closed contour.

Following [15] there is the alternative calculation

$$dA = 2\pi x (1 - x^2 \kappa_p^2)^{-1/2} dx \quad (2.60)$$

2.5.2 Program testing

Like for the 2-D properties, it is equally important to test the programmed code for the 3-D ones. First, take a circle with radius $r = 2$ ($Ax_1 = By_1 = 2$) and compare the output with the result of the formulas $S = 4\pi r^2$ for the surface of a sphere and $V = \frac{4}{3}\pi r^3$ for its volume.

Plugging the principal curvatures from equation (2.27) and (2.55) into equation (2.49) for the Gaussian curvature and into (2.51) for the mean curvature leads to

$$K = \frac{y''x'|x'| - y'|x'|x''}{|y|(x'^2 + y'^2)^2} \quad (2.61)$$

$$H = \frac{1}{2} \frac{|y|(y''x' - y'x'') + |x'|(x'^2 + y'^2)}{|y|(x'^2 + y'^2)^{3/2}} \quad (2.62)$$

These formulas uses the program for its calculations and their results are therefore compared to the analytic solutions. Table 2.5 shows the results for the sphere. The ellipsoid with semi-axes a, b and c is a good non-uniform curved object to test the program. As rotational symmetry is assumed, the ellipsoid becomes a spheroid and $b = c$. A spheroid's volume is $V = 4/3\pi ab^2$. For its surface the calculation differs between a prolate ($a > b$) and an oblate ($a < b$) one.

Sphere ($r = 2$)	program output	analytic solution
Surface	50.2655	$4\pi(2)^2 \approx 50.2655$
Volume	33.5103	$\frac{4}{3}\pi(2)^3 \approx 33.5103$
Gaussian curvature	0.25	0.25
Mean curvature	0.5	0.5

Table 2.5: Comparison of the program output with the analytical result for the sphere. Surface, volume, Gaussian and Mean curvature are compared and approve the correctness of the calculations.

Using the notation from *WolframMathWorld*, the surface of a prolate spheroid is

$$S = 2\pi b^2 + \frac{2\pi ab}{e} \arcsin(e) \quad (2.63)$$

where $e = \sqrt{\frac{a^2-b^2}{a^2}}$ denotes the ellipticity and ($a > b$). In the case of an oblate spheroid, the formula becomes

$$S = 2\pi b^2 + \frac{2\pi a^2}{e} \ln\left(\frac{1+e}{1-e}\right) \quad (2.64)$$

In this case the ellipticity $e = \sqrt{\frac{b^2-a^2}{b^2}}$ and naturally ($a < b$). The results therefor can be seen in Table 2.6. The Gaussian and mean curvature for a non-uniform curved object like the spheroid are obviously different from point to point and are compared in the graphs seen in Figure 2.19. It is sufficient to use a 2-dimensional plot, because κ_p remains constant for every fixed parameter t (due to the rotational symmetry). The continuously plotted curves refer to the curvatures calculated by the program, the circles and diamonds are derived by an analytic calculation using the formulas

$$K = \frac{4a^2}{[b^2 + a^2 + (b^2 - a^2) \cos(2t)]^2} \quad (2.65)$$

for the Gaussian curvature of a spheroid and

$$H = \frac{a[3b^2 + a^2 + (b^2 - a^2) \cos(2t)]}{\sqrt{2} \cdot b \cdot [b^2 + a^2 + (b^2 - a^2) \cos(2t)]^{3/2}} \quad (2.66)$$

for its mean curvature. The same notation is used as before (a, b : semi-axes; t : parameter).

2.5.3 Alignment

Before we can rotate the contour however, we have to assure that the long axis is aligned with the x -axis. Therefor we can calculate the covariance matrix

$$\mathbf{V} = \begin{pmatrix} \text{cov}(X, X) & \text{cov}(X, Y) \\ \text{cov}(X, Y) & \text{cov}(Y, Y) \end{pmatrix} \quad (2.67)$$

where $\text{cov}(X, Y) = \sum_{i=1}^N \frac{(x_i - \bar{x})(y_i - \bar{y})}{N}$, and then search for the eigenvector with the larger eigenvalue. This vector is along the long axis of the contour, which

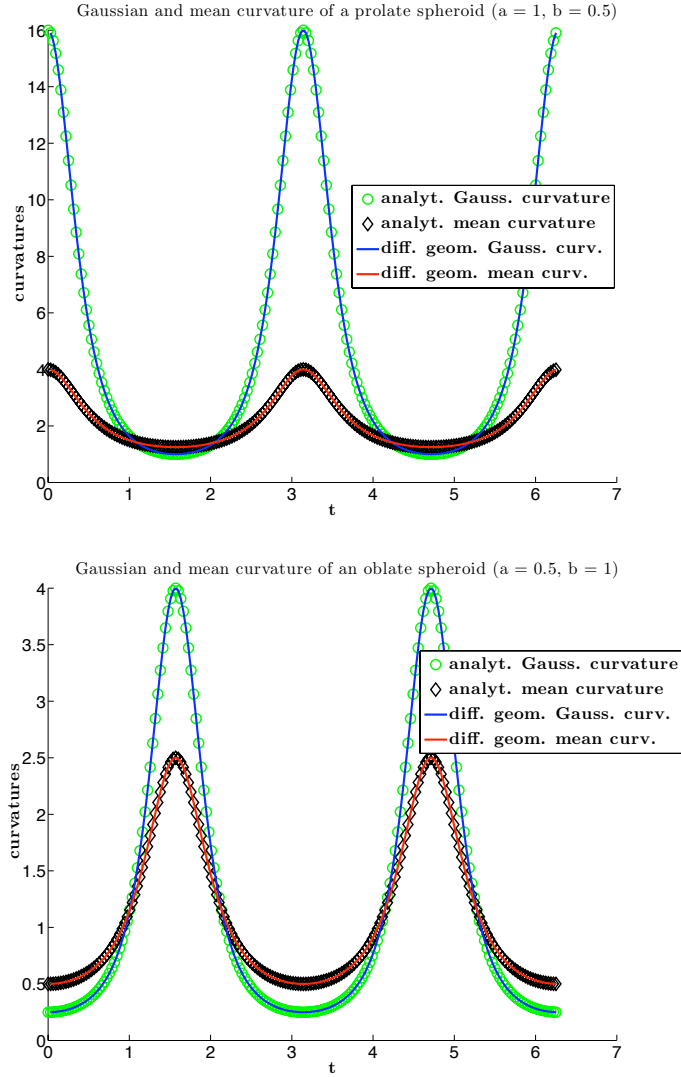


Figure 2.19: Comparison of the program output [using the formulas (2.61) and (2.62)] with the analytically derived results [given by equations (2.65) and (2.66)] for the Gaussian and mean curvature. The upper graph shows the results for a prolate spheroid ($a = 1, b = 0.5$), the lower graph for an oblate one ($a = 0.5, b = 1$). The blue line denotes the Gaussian curvature calculated by differential geometry and matches well the analytical solutions (green circles). The same does apply to the red line and the black diamonds that express the mean curvature in both cases respectively

Spheroid ($a = 1, b = 0.5$) \rightarrow prolate	program output	analytic solution
Surface	5.3696	5.3696
Volume	1.0472	$\frac{4}{3}\pi \cdot 1 \cdot (0.5)^2 \approx 1.0472$
Spheroid ($a = 0.5, b = 1$) \rightarrow oblate	program output	analytic solution
Surface	8.6719	8.6719
Volume	2.0944	$\frac{4}{3}\pi \cdot 0.5 \cdot (1)^2 \approx 2.0944$

Table 2.6: Comparison of the program output with the analytical result for a prolate and an oblate spheroid. In both cases the surface as well as the volume are compared and the results coincide.

has to be rotated to the x -axis. Or we can follow Khairy [43] and therewith Brechbühler [7] in finding the translational and rotational invariant form. The object is rotated to canonical positions in parameter space and in object space. The set of parametric equations for a general ellipse is written

$$\vec{p}(t) = \begin{pmatrix} x(t) \\ y(t) \end{pmatrix} = \begin{pmatrix} A_1^x & B_1^x \\ A_1^y & B_1^y \end{pmatrix} \cdot \begin{pmatrix} \sin(t) \\ \cos(t) \end{pmatrix} = \begin{pmatrix} A_1^x \sin(t) + B_1^x \cos(t) \\ A_1^y \sin(t) + B_1^y \cos(t) \end{pmatrix} \quad (2.68)$$

where the matrix of coefficients

$$\mathbf{M} = \begin{pmatrix} A_1^x & B_1^x \\ A_1^y & B_1^y \end{pmatrix} \quad (2.69)$$

determines the length of the semi-axes and the orientation of the ellipse in the coordinate system. The matrix $\mathbf{H} = \mathbf{M}^T \cdot \mathbf{M}$ has to be rotated into its principal axis system by transforming it into a diagonal matrix. More precisely it is

$$\mathbf{H} = \begin{pmatrix} a & c \\ c & b \end{pmatrix} = \begin{pmatrix} [A_1^x]^2 + [A_1^y]^2 & A_1^x B_1^x + A_1^y B_1^y \\ B_1^x A_1^x + B_1^y A_1^y & [B_1^x]^2 + [B_1^y]^2 \end{pmatrix} = \mathbf{M}^T \cdot \mathbf{M} \quad (2.70)$$

what yields

$$a = [A_1^x]^2 + [A_1^y]^2 \quad b = [B_1^x]^2 + [B_1^y]^2 \quad c = A_1^x B_1^x + A_1^y B_1^y \quad (2.71)$$

That is the direct connection to the general ellipse equation

$$ax^2 + by^2 + 2cxy = 0 \quad (2.72)$$

where indeed the equations (2.71) hold and $c = 0$ then gives the canonical form with the length of the semi-axes $\frac{1}{\sqrt{a}}$ and $\frac{1}{\sqrt{b}}$.

3

Conclusions and Outlook

So far the described methods work and we take advantage of incorporating additional knowledge about the assumed closeness and smoothness of the membrane into our calculations. The expected behavior plotting the area and the bending energy over time would be some remarkable change coincident with an additional force acting on the nucleus. The additional force could be integrated into equation (2.53) by an additional Lagrange multiplier [14], respecting the additional constraint on the length along the x -axis. The new energy functional to minimize then would be

$$F_{H-C} = \oint_{surface} \left[\frac{k_b}{2} (2H)^2 - k_b 2HC_0 + \sigma \right] dA - pV - fL \quad (3.1)$$

where f is the additional force (and simultaneously the new Lagrange multiplier) and L the overall length of the nucleus. This force is most likely exerted by the mitotic spindle, as explained in section 1.2.1 and it is shown [47] that this force only can be assigned to a broad area of the membrane by a spindle properly anchored at the SPB. Otherwise the membrane tries to minimize surface area at the expense of high curvature regions, yielding to tether formation. The same reason should hold for the formation of the tube in the dumbbell-shape. The curious thing about the visibility of the tube connecting the two bulbs in the dumbbell-shape stage is (see Figure 1.4 on page 7) that there is often no signal, although it should be $\approx \frac{1}{4}$ of the intensity of the bulb region considering the bare membrane material (see also section 1.2.2). Hereby a tube diameter of ≈ 100 nm (enough for 6-8 MT's) is assumed and the fact that the tube is not always in the focus plane of the LSCM. But even without any signal, the algorithm completes the dumbbell, showing its full supremacy compared to classical segmentation methods. The delicate part here is to avoid self-intersection, which can easily occur dealing with shapes similar to Figure 2.5(d). The pareto-optimum including the bending energy delightfully avoids sharp edges and cusps by smoothing the surface, but there is no elegant way to inhibit self-intersection. At the cost of computationally expensive calculations however, we can impede it. The occurrence of turnings at the transition from the bulb to the tube will provoke overshootings, even using a huge amount of coefficients. They can indeed be suppressed using Lanczos sigma factor, as explained in section 2.1.1.

In summary we will calculate the surface area and the enclosed volume of the observed nuclei and use them as constraints on the free energy function mini-

mization like outlined before. After minimization we expect to get shapes very similar to the observed ones until a certain time during morphogenesis (for example after the peanut-like shape) where the observed shape differs from the 'natural' minimal energy shape. This is the time where new constraints must occur. An experiment to prove the idea of the spindle being mainly responsible would be to cut the spindle of a dumbbell-shaped nucleus by laser ablation and to see if the nucleus shrinks back to an earlier stage. The central assumption of the model is that the nucleus assumes a shape that minimizes its overall membrane energy subject to the appropriate constraints, first without the additional length constraint, then including it.

Regarding the nuclear envelope like an artificial vesicle may be too simple as the nuclear membrane embeds other proteins like the NPC or consist of different types of lipids and therefore may be spatially inhomogeneous. But taking two different molecular species, it has been shown that it simply rescales the elastic parameters of the membrane [14].

Additionally to the very useful investigation of the fission yeast nucleus, there is a wide field of possible applications for our method describing shapes. It could be used for an automated pollen recognition like in [63] where fluorescence microscopy is used to image the pollen. The description in terms of coefficients should be sensitive enough to distinguish between them. The registration of plant leaves using shape analysis [51] where Kuhl and Giardina's method [45] was successfully applied is another example, or thinking of *C. elegans* embryos with a non-uniformly distributed signal, our method could also be very helpful. It is a very promising project, where further investigation is worthwhile.

The presented work makes it possible to use equation (3.1) and subsequently is a tool to derive forces based on images ! When we will have determined the forces, we can prove or reject the idea of the mitotic spindle applying the main force that drives the spatial division of the forming daughter nuclei or rather where other or additional mechanisms have to participate. The answer to this question will be a big step forward in understanding the cell cycle and a long awaited push giving rise to further investigations. We have developed a new method that is particularly suitable for image processing of confocal images, that especially occur in a wide range of life sciences, but is generally applicable for any pattern recognition in terms of determining shapes.

Appendix A

Protocol

Protocol for 1liter of **EMM** (Edinburgh Minimal Medium):

3 g	$\text{C}_8\text{H}_5\text{KO}_4$
2.2 g	Na_2HPO_4
5 g	NH_4Cl
20 g	Glucose \rightarrow final concentration: 2%
20 ml	50x salt solution
1 ml	solution A1(minerals)
1 ml	solution A2a (vitamins)
1 ml	solution A2b
(20 g	agar for the plates)

wherein the solutions consist of the following:

A1:	5 g/l	boric acid	80.9 mM
	4 g/l	MnSO_4	23.7 mM
	4 g/l	$\text{ZnSO}_4 \cdot 7\text{H}_2\text{O}$	13.9 mM
	2 g/l	$\text{FeCl}_2 \cdot 6\text{H}_2\text{O}$	7.40 mM
	0.4 g/l	molybdic acid	2.47 mM
	1 g/l	KI	6.02 mM
	0.4 g/l	$\text{CuSO}_4 \cdot 5\text{H}_2\text{O}$	1.60 mM
A2a:	1 g/l	pantothenic acid	4.20 mM
	10 g/l	nicotinic acid	81.2 mM
A2b:	10 g/l	inositol	55.5 mM
	10 mg/l	biotin	40.8 μM

Appendix B

List of abbreviations

S phase	synthesis phase
G _{1, 2} phase	gap phase 1, 2
M phase	mitotic phase
MT	microtubule
MTOC	microtubule-organizing centers
SPB	spindle pole body
NE	nuclear envelope
Klp	kinesin-like proteins
GFP	Green fluorescent protein
SOI	structure of interest
NPC	nuclear pore complex
LSCM	laser scanning confocal microscope
PSF	point spread function
FWHM	full-width-half-maximum
NA	numerical aperture
PMT	photomultiplier tube
EMM	Edinburgh Minimal Medium
FS	Fourier series
MR	magnetic resonance
ADE	area difference elasticity

Bibliography

- [1] Gene database. URL <http://www.genedb.org/>.
- [2] Stephen A. Adam. The nuclear pore complex. *Genome Biology*, 2(9):reviews00007.1–00007.6, August 2001.
- [3] Bruce Alberts, Dennis Bray, Alexander Johnson, Julian Lewis, Martin Raff, Keith Roberts, and Peter Walter. *Essential cell biology*. Garland Publishing, 1998.
- [4] Bruce Alberts, Alexander Johnson, Julian Lewis, Martin Raff, Keith Roberts, and Peter Walter. *Molecular biology of the cell*. Garland Science, 2002.
- [5] C. Bauer, V. Herzog, and M.F. Bauer. Improved technique for electron microscope visualization of yeast membrane structure. *Microsc Microanal*, 7(6):530–534, 2001.
- [6] Ronald N. Bracewell. *Fourier analysis and imaging*. Kluwer Academic, 2003.
- [7] Ch. Brechbühler, G. Gerig, and O. Kübler. Parametrization of closed surfaces for 3-d shape description. *Computer Vision and Image Understanding*, 61(2):154–170, 1995.
- [8] I.N. Bronstein, K.A. Semendjajew, G. Musiol, and H. Mühlig. *Taschenbuch der Mathematik*. Verlag Harri Deutsch, 2000.
- [9] P. B. Canham. The minimum energy of bending as a possible explanation of the biconcave shape of the human red blood cell. *Journal of Theoretical Biology*, 26(1):61–81, 1970.
- [10] Yair Censor. Pareto optimality in multiobjective problems. *Applied Mathematics and Optimization*, 4(1):41–59, 1977.
- [11] Thomas F. Coleman and Yuying Li. On the convergence of interior-reflective newton methods for nonlinear minimization subject to bounds. *Mathematical Programming*, 67(1-3):189–224, 2005.
- [12] Harold S. M. Coxeter. *Unvergängliche Geometrie*. Birkhäuser, 1981.
- [13] N. O. Da Cunha and E. Polak. Constrained minimization under vector-valued criteria in finite dimensional spaces. *Journal of Mathematical Analysis and Applications*, 19:103–124, 1967.

- [14] I. Derényi, G. Koster, M. M. van Duijn, A. Czövek, M. Dogterom, and J. Prost. Membrane nanotubes. *Controlled Nanoscale Motion*, pages 141–159, 2007.
- [15] H.J. Deuling and W. Helfrich. Red blood cell shapes as explained on the basis of curvature elasticity. *Biophys J*, 16(8):861–8, 1976.
- [16] R Ding, KL McDonald, and JR McIntosh. Three-dimensional reconstruction and analysis of mitotic spindles from the yeast, *Schizosaccharomyces pombe*. *J. Cell Biol.*, 120(1):141–151, 1993.
- [17] R Ding, RR West, DM Morphew, BR Oakley, and JR McIntosh. The spindle pole body of *Schizosaccharomyces pombe* enters and leaves the nuclear envelope as the cell cycle proceeds. *Mol. Biol. Cell*, 8(8):1461–1479, 1997.
- [18] Bernard Diu, Claudine Guthmann, Danielle Lederer, and Bernard Roulet. *Physique statistique*. Hermann, 1989.
- [19] Manfredo P. do Carmo. *Differentialgeometrie von Kurven und Flächen*. Vieweg, 1992.
- [20] H.-G. Döbereiner, E. Evans, M. Kraus, U. Seifert, and M. Wortis. Mapping vesicle shapes into the phase diagram: A comparison of experiment and theory. *Phys. Rev. E*, 55(4):4458–4474, Apr 1997.
- [21] F. Dyson. A meeting with enrico fermi. *Nature*, 427(22):297, January 2004.
- [22] Richard Egel. *The Molecular Biology of Schizosaccharomyces pombe*. Springer-Verlag Berlin, 2004.
- [23] H. Eviatar and R. L. Somorjai. A fast, simple active contour algorithm for biomedical images. *Pattern Recogn. Lett.*, 17(9):969–974, 1996.
- [24] Rida T. Farouki and Hwan Pyo Moon. Bipolar and multipolar coordinates. In *IMA Conference on the Mathematics of Surfaces*, pages 348–371. Springer-Verlag, 2000.
- [25] Torsten Fließbach. *Elektrodynamik - Lehrbuch zur theoretischen Physik*, volume 3. Spektrum Akademischer Verlag, 2005.
- [26] E. J. Garboczi. Three-dimensional mathematical analysis of particle shape using x-ray tomography and spherical harmonics: Application to aggregates used in concrete. *Cement and Concrete Research*, 32(10):1621–1638, 2002.
- [27] Charles R. Giardina and Frank P. Kuhl. Accuracy of curve approximation by harmonically related vectors with elliptical loci. *Computer Graphics and Image Processing*, 6(3):277–285, June 1977.
- [28] Johan Gielis. A generic geometric transformation that unifies a wide range of natural and abstract shapes. *Am. J. Bot.*, 90(3):333–338, 2003.
- [29] Yuko Giga-Hama and Hiromichi Kumagai. *Foreign Gene Expression in Fission Yeast Schizosaccharomyces pombe*. Springer-Verlag Berlin and Landes Bioscience Georgetown, 1997.

- [30] F Gittes, B Mickey, J Nettleton, and J Howard. Flexural rigidity of microtubules and actin filaments measured from thermal fluctuations in shape. *J. Cell Biol.*, 120(4):923–934, 1993.
- [31] Alfred Gray. *Differentialgeometrie, Klassische Theorie in moderner Darstellung*. Spektrum Akademischer Verlag, 1994.
- [32] Alfred Gray, Elsa Abbena, and Simon Salamon. *Modern Differential Geometry of Curves and Surfaces with Mathematica*. Chapman and Hall / CRC Press, 2006.
- [33] Walter Greulich. *Lexikon der Physik (Band 2)*. Spektrum Akademischer Verlag, 1999.
- [34] IM Hagan. The fission yeast microtubule cytoskeleton. *J Cell Sci*, 111(12):1603–1612, 1998.
- [35] P.C. Hansen. The l-curve and its use in the numerical treatment of inverse problems. In *Invite Computational Inverse Problems in Electrocardiology*. WIT Press, 2000.
- [36] Per Christian Hansen. *Rank-deficient and discrete ill-posed problems: numerical aspects of linear inversion*. Society for Industrial and Applied Mathematics, Philadelphia, PA, USA, 1998.
- [37] W Helfrich. Elastic properties of lipid bilayers: theory and possible experiments. *Z Naturforsch [C]*, 28(11):693–703, 1973.
- [38] R M Hochmuth and R E Waugh. Erythrocyte membrane elasticity and viscosity. *Annual Review of Physiology*, 49(1):209–219, 1987.
- [39] Joe Howard and Anthony A. Hyman. Dynamics and mechanics of the microtubule plus end. *Nature*, 422(6933):753–758, 2003.
- [40] Stephen Hyde, Sten Andersson, Kåre Larsson, Zoltan Blum, Tomas Landh, Sven Lidin, and Barry W. Ninham. *The language of shape*. Elsevier Science B.V., 1997.
- [41] Alan Isaacs. *A dictionary of physics*. Oxford University Press, 2003.
- [42] M. Kass, A. Witkin, and D. Terzopoulos. Snakes: Active contour models. *International Journal of Computer Vision*, 1:321–331, 1988.
- [43] Khaled Khairy and Jonathon Howard. Spherical harmonics-based parametric deconvolution of 3d surface images using bending energy minimization. *Medical Image Analysis*, In Press, Corrected Proof:–, 2007.
- [44] Ulrich Kilian and Christine Weber. *Lexikon der Physik (Band 4)*. Spektrum Akademischer Verlag, 2000.
- [45] Frank P. Kuhl and Charles R. Giardina. Elliptic fourier features of a closed contour. *Computer Graphics and Image Processing*, 18:236–258, 1982.
- [46] Jeffrey C. Lagarias, James A. Reeds, Margaret H. Wright, and Paul E. Wright. Convergence properties of the nelder–mead simplex method in low dimensions. *SIAM Journal on Optimization*, 9(1):112–147, 1998.

- [47] Gerald Lim H. W., Greg Huber, Yoshihiro Torii, Aiko Hirata, Jonathan Miller, and Shelley Sazer. Vesicle-like biomechanics governs important aspects of nuclear geometry in fission yeast. *PLoS ONE*, 2(9):e948, Sep 2007.
- [48] J. Lippincott-Schwartz and G.H. Patterson. Development and use of fluorescent protein markers in living cells. *Science*, 300(5616):87–91, 2003.
- [49] Martin M. Lipschutz. *Theory and problems of differential geometry*. McGraw-Hill, 1969.
- [50] Harvey Lodish, Arnold Berk, S. Lawrence Zipursky, Paul Matsudaira, David Baltimore, and James Darnell. *Molecular cell biology*. W. H. Freeman and Company, 2000.
- [51] Tracy McLellan. The roles of heterochrony and heteroblasty in the diversification of leaf shapes in *Begonia dregei* (begoniaceae). *American Journal of Botany*, 80(7):796–804, jul 1993.
- [52] J S Miles. Structurally and functionally conserved regions of cytochrome p-450 reductase as targets for dna amplification by the polymerase chain reaction. cloning and nucleotide sequence of the *Schizosaccharomyces pombe* cDNA. *Biochem J*, 287 (Pt 1):195–200, 1992.
- [53] Ranjan Mukhopadhyay, Gerald Lim H. W., and Michael Wortis. Echinocyte Shapes: Bending, Stretching, and Shear Determine Spicule Shape and Spacing. *Biophys. J.*, 82(4):1756–1772, 2002.
- [54] Anne Paoletti and Phong T. Tran. Anchoring microtubules at the spindle poles. *Nat Cell Biol*, 9(6):619–621, 2007.
- [55] Mercedes Pardo and Paul Nurse. The nuclear rim protein Amo1 is required for proper microtubule cytoskeleton organisation in fission yeast. *J Cell Sci*, 118(8):1705–1714, 2005.
- [56] James B. Pawley. *Handbook of biological confocal microscopy*. Kluwer Academic, 1995.
- [57] James B. Pawley. *Handbook of biological confocal microscopy*. Springer Science and Business Media, 2006.
- [58] J. Pécureaux, C. Zimmer, and J-C. Olivo-Marin. Biophysical active contours for cell tracking i: Tension and bending. *IEEE International Conference on Image Processing, 2006*, pages 1949–1952, 8-11 Oct. 2006.
- [59] Eric Persoon and King-Sun Fu. Shape discrimination using fourier descriptors. *IEEE Transactions on systems, man and cybernetics*, SMC-7(3):170–179, March 1977.
- [60] William H. Press, Saul A. Teukolsky, William T Vetterling, and Brian P. Flannery. *Numerical Recipes in C++*. Cambridge University Press, 2002.
- [61] W. Rawicz, K. C. Olbrich, T. McIntosh, D. Needham, and E. Evans. Effect of Chain Length and Unsaturation on Elasticity of Lipid Bilayers. *Biophys. J.*, 79(1):328–339, 2000.

- [62] G. Rodriguez and D. Theis. An algorithm for estimating the optimal regularization parameter by the l-curve. *Rendiconti di Matematica*, 25(7):69–84, 2005.
- [63] Olaf Ronneberger, Eckhart Schultz, and Hans Burkhardt. Automated pollen recognition using 3d volume images from fluorescence microscopy. *Aerobiologia*, 18:107–115(10), June 2002.
- [64] M P Rout and J D Aitchison. The nuclear pore complex as a transport machine. *J Biol Chem*, 276(20):16593–16596, 2001.
- [65] David J. Sharp, Kent L. McDonald, Heather M. Brown, Heinrich J. Matthies, Claire Walczak, Ron D. Vale, Timothy J. Mitchison, and Jonathan M. Scholey. The bipolar kinesin, klp61f, cross-links microtubules within interpolar microtubule bundles of drosophila embryonic mitotic spindles. *J. Cell Biol.*, 144(1):125–138, 1999.
- [66] Ian Naismith Sneddon. *Fourier Series*. Routledge and Kegan Paul, 1961.
- [67] Michael Spivak. *A comprehensive introduction to differential geometry, volume 1*. Number 332 in 332. Publish or Perish, 1979.
- [68] Gabor Szekely, Andras Kelemen, Christian Brechbuhler, and Guido Gerig. Segmentation of 2-d and 3-d objects from mri volume data using constrained elastic deformations of flexible fourier contour and surface models. *Medical Image Analysis*, 1(1):19–34, 1996.
- [69] Iva M. Tolic-Nørrelykke, Leonardo Sacconi, Genevieve Thon, and Francesco S. Pavone. Positioning and elongation of the fission yeast spindle by microtubule-based pushing. *Current Biology*, 14(13):1181–1186, 2004.
- [70] Kazunori Tomita and Julia Promisel Cooper. The telomere bouquet controls the meiotic spindle. *Cell*, 130:113–126, July 2007.
- [71] Mika Toya, Masamitsu Sato, Uta Haselmann, Kazuhide Asakawa, Damian Brunner, Claude Antony, and Takashi Toda. [gamma]-tubulin complex-mediated anchoring of spindle microtubules to spindle-pole bodies requires msd1 in fission yeast. *Nat Cell Biol*, 9(6):646–653, 2007.
- [72] C. R. Vogel. Non-convergence of the L-curve regularization parameter selection method . *Inverse Problems*, 12:535–547, August 1996.
- [73] J. Wei. Least square fitting of an elephant. *Chemtech*, 5:128–129, 1975.
- [74] Eric W. Weisstein. Mathworld. URL <http://mathworld.wolfram.com>.
- [75] R R West, E V Vaisberg, R Ding, P Nurse, and J R McIntosh. cut11(+): A gene required for cell cycle-dependent spindle pole body anchoring in the nuclear envelope and bipolar spindle formation in schizosaccharomyces pombe. *Mol Biol Cell*, 9(10):2839–2855, 1998.
- [76] T. Wilson and C. Sheppard. *Theory and practice of scanning optical microscopy*. London: Academic Press, —c1984, 1984.

- [77] Liling Zheng, Cindi Schwartz, Valentin Magidson, Alexey Khodjakov, and Snezhana Oliferenko. The spindle pole bodies facilitate nuclear envelope division during closed mitosis in fission yeast. *PLoS Biology*, 5(7), 2007.

Acknowledgements

This interesting project was a marvellous experience, I evolved so much and I am glad to have received support from so many people. I want to thank strongly Dr. Khaled Khairy for supervising my project and many helpful discussions. His leaving in the middle of the project provoked a great loss. I am deeply thankful to Prof. Jonathon Howard for giving me the opportunity to realize this project. I learned so much from his expertise and advice. I highly appreciate Dr. Iva Marija Tolić-Nørrelykke who really always wanted my best and helped me in all biological questions. Many thanks to Prof. Petra Schulle for being available as the second referee.

I am greatly delighted to Isabel Raabe for patiently introducing me to *S. pombe* culturing and imaging as well as reviewing the biological sections. Especially I am beholden to Jacques Pecreaux and Marzuk Kamal for always assisting me - especially in programming and methodical questions. Many thanks to Horatiu Fantana and Henning Urban for valuable tips improving my OS and LaTeX skills and together with Susanne Bechstedt for wonderful conversations, creating a very pleasing ambience. I thank Henri Saleh for benefit in any computational question and Matt Boes for technical support. As a matter of course I want to thank the whole Howard-Lab and the Tolić-Nørrelykke-Lab for invariably providing support and a good atmosphere.

Declaration

I herewith declare that I have produced this paper without the prohibited assistance of third parties and without making use of aids other than those specified; notions taken over directly or indirectly from other sources have been identified as such. This paper has not previously been presented in identical or similar form to any other german or foreign examination board. The thesis work was conducted from 21/12/2006 to 12/02/2008 under the supervision of Prof. Dr. Jonathon Howard and Dr. Khaled Khairy at the Max Planck Institute of Molecular Cell Biology and Genetics in Dresden, Germany.

Hiermit versichere ich, dass ich die vorliegende Arbeit ohne unzulässige Hilfe Dritter und ohne Benutzung anderer als der angegebenen Hilfsmittel angefertigt habe; die aus fremden Quellen direkt oder indirekt übernommenen Gedanken sind als solche kenntlich gemacht. Die Arbeit wurde bisher weder im Inland noch im Ausland in gleicher oder ähnlicher Form einer anderen Prüfungsbehörde vorgelegt. Die vorliegende Arbeit wurde vom 21.12.2006 bis 12.02.2008 unter der Aufsicht von Prof. Dr. Jonathon Howard und Dr. Khaled Khairy am Max Planck Institut für Molekulare Zellbiologie und Genetik in Dresden durchgeführt.

Dresden, February 2008

Jürgen Mayer